

JGR Space Physics

RESEARCH ARTICLE

10.1029/2020JA027923

Key Points:

- Report on ionosonde observations and Global Navigation Satellite System estimated total electron contents for the 2 July 2019 solar eclipse
- Low-latitude modeling of ionospheric characteristics leads to the hypothesis of an equatorial prereversal enhanced electric field
- Differences from previous observations for other solar eclipses and the effects of the reference selection procedure are discussed

Correspondence to:

M. Bravo,
mbravo@dgeo.udec.cl

Citation:

Bravo, M., Martínez-Ledesma, M., Foppiano, A., Urrea, B., Ovalle, E., Villalobos, C., et al. (2020). First report of an eclipse from Chilean ionosonde observations: Comparison with total electron content estimations and the modeled maximum electron concentration and its height. *Journal of Geophysical Research: Space Physics*, 125, e2020JA027923. <https://doi.org/10.1029/2020JA027923>

Received 20 FEB 2020

Accepted 15 JUL 2020

Accepted article online 6 AUG 2020

First Report of an Eclipse From Chilean Ionosonde Observations: Comparison With Total Electron Content Estimations and the Modeled Maximum Electron Concentration and Its Height

M. Bravo^{1,2} , M. Martínez-Ledesma^{3,4} , A. Foppiano^{1,2} , B. Urrea¹ , E. Ovalle^{1,2} , C. Villalobos^{2,5} , J. Souza⁶ , E. Carrasco¹ , P. R. Muñoz^{2,7} , L. Tamblay^{2,7} , P. Vega-Jorquera^{2,7} , J. Marín^{2,7} , R. Pacheco^{2,7} , E. Rojo^{2,8} , R. Leiva^{2,8} , and M. Stepanova³ 

¹Departamento de Geofísica, Universidad de Concepción, Concepción, Chile, ²Centro Interuniversitario de Física de la Alta Atmósfera, Chile, ³Departamento de Física, Universidad de Santiago de Chile, Santiago, Chile, ⁴CePIA, Departamento de Astronomía, Universidad de Concepción, Concepción, Chile, ⁵Facultad de Educación y Ciencias Sociales, Universidad Adventista de Chile, Chillán, Chile, ⁶Instituto Nacional de Pesquisas Espaciais, INPE, São José dos Campos, Brazil, ⁷Departamento de Física y Astronomía, Universidad de La Serena, La Serena, Chile, ⁸Facultad de Ingeniería y Negocios, Universidad Adventista de Chile, Chillán, Chile

Abstract The ionospheric responses to the total solar eclipse on 2 July 2019 over low latitudes in southern South America are presented. Ionosonde observations were used within the totality path at La Serena (LS: 29.9°S, 71.3°W) and at Tucumán (TU: 26.9°S, 65.4°W) and Jicamarca (JI: 12.0°S, 76.8°W), with 85% and 52% obscuration, respectively. Total electron content (TEC) estimations over the South American continent were analyzed. The ionospheric impact of the eclipse was simulated using the Sheffield University Plasmasphere-Ionosphere Model (SUPIM) at the Instituto Nacional de Pesquisas Espaciais (INPE). The significant variability of the diurnal variations of the various ionospheric characteristics over equatorial and low latitudes on geomagnetically quiet days makes it difficult to unambiguously determine the ionospheric responses to the eclipse. Nonetheless, some specific issues can be derived, mainly using simulation results. The *E* and *F1* layer critical frequencies and densities below 200 km are found to consistently depend on decreasing solar radiation. However, the *F1* layer stratification observed at both TU and LS cannot be related to the eclipse or other processes. The *F2* layer does not follow the changes in direct solar radiation during the eclipse. The SUPIM-INPE-modeled *F* region critical frequency and TEC are overestimated before the eclipse at LS and particularly at TU. However, these overestimations are within the observed large day-to-day variability. When an artificial prereversal enhancement is added, the simulations during the eclipse better reproduce the observations at JI, are qualitatively better for LS, and are out of phase for TU. The simulations are consistent with conjugate location effects.

1. Introduction

The ionosphere, the conductive region of the upper atmosphere located above approximately 60 km, is composed of a minority of free electrons and ions among a majority of neutral molecular and atomic particles. Ionospheric plasma is mainly produced by the absorption of extreme ultraviolet and X-ray solar radiation by neutral gases, which prevent this type of radiation from reaching the middle and lower atmosphere. During a total solar eclipse, the moon blocks solar radiation regularly and predictably (Zirker, 1980), forcing a gradual shadowing condition that can be used to empirically determine the internal characteristics and dynamics of the ionosphere. However, solar radiation cannot be considered a uniform source of ionization, and the ionosphere cannot be assumed to be a perfect detector (Rishbeth, 1968). The impacts of a solar eclipse can depend on the previous state of the ionosphere (which differs among various regions), the internal dynamics and transport of plasma, the external forcing (i.e., space weather activity and lower atmospheric interactions), and the eclipse itself. Many studies have focused on solar eclipses to improve our understanding of the characteristics and dynamics of the ionosphere. Appendix A gives a summary of the results from observational and modeling studies of solar eclipses from 1920 up to the 21 August 2017

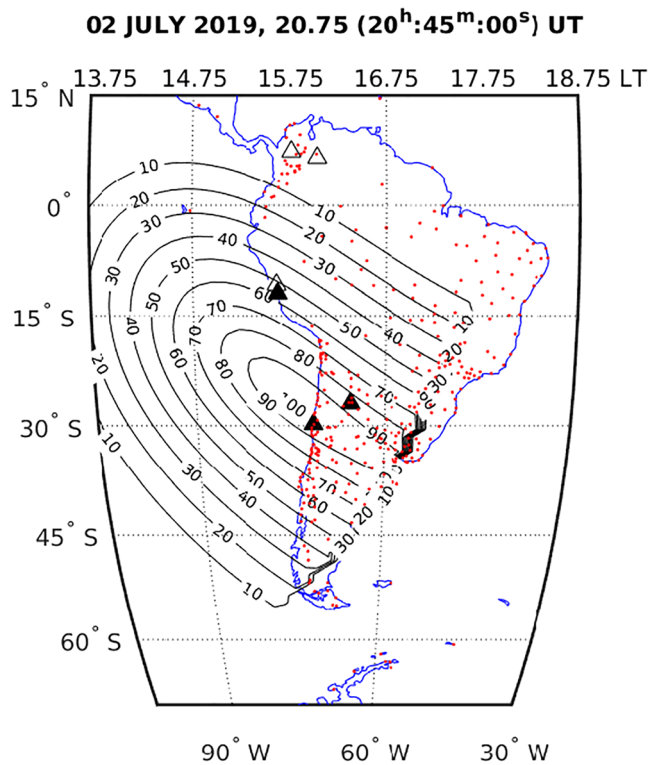


Figure 1. Ionosondes (black triangles), GNSS receivers (red dots), and geomagnetic conjugate locations of ionosondes (open triangles). Eclipse's obscuration mask (black lines, obscuration %) at the maximum occultation time over La Serena (29.9°S, 71.3°W) at 300 km altitude.

so-called Great American Eclipse, which is by far the best described and most interpreted solar eclipse to date.

In the last two decades, ionospheric observations in South America have increased significantly. This is particularly true in Chile, where there has been a tenfold increase in the number of dual-frequency Global Navigation Satellite System (GNSS) receivers set up by the Centro Sismológico Nacional (National Seismological Centre, CSN in Spanish). Furthermore, a new ionospheric station was recently deployed in northern Chile. In this paper, the ionospheric response to the solar eclipse of 2 July 2019 is determined using ionosonde observations within the total obscuration path over La Serena (29.9°S, 71.3°W) and total electron content (TEC) observations over South America obtained using networks of GNSS receivers. The ionosonde measurements are also compared with observations from stations located in Tucumán (26.9°S, 65.4°W) and Jicamarca (12.0°S, 76.8°W) to determine the impacts at different locations. In addition, the response is modeled to further understand the impacts on the ionosphere and to determine both the modeling goodness and the ways in which the model used herein can be improved.

2. Materials and Methods

2.1. The Solar Eclipse on 2 July 2019

The solar eclipse on 2 July 2019 was observed over most of South America. The path of totality began over the Pacific Ocean, traversed the continent starting near La Serena in Chile (29.9°S, 71.3°W) at 20.63 UT (SAT = 15.8), and ended near Buenos Aires (34.6°S, 58.3°W), Argentina, at 20.73 UT (SAT = 16.8), close to sunset. At La Serena, a partial solar eclipse was first observed at 19.37 UT (SAT = 14.6) and ended at 21.77 UT (SAT = 17.0).

The total duration at La Serena was approximately 2 min and 36 s. The

eclipse occurred during an extended period of quiet geomagnetic activity conditions and very low solar activity (15 quiet days between June 29 and July 20 with $Kp \leq 2^+$ and the observed $F10.7$ index ≤ 70).

An eclipse obscuration mask at 300 km altitude is depicted in Figure 1. This obscuration mask is calculated at the time of eclipse totality at sea level over La Serena (29.9°S, 71.3°W). The obscuration mask shows the effect of the percent reduction in solar radiation at different locations at the approximate altitude, which would correspond to the maximum ionospheric concentration. The obscuration mask was computed using a script based on the code of Frissell (2017) that uses the Astropy python project library (<https://www.astropy.org/>) to calculate the geometry of the solar occultation at different locations on Earth and the corresponding percent reduction in solar radiation. The mask values are calculated every 30 s with a latitudinal and longitudinal resolution of 0.25°. Since the geometry of the eclipse occultation at 300 km is different from that at ground level (Stankov et al., 2017; Verhulst & Stankov, 2020), the shadowing at this altitude is delayed by approximately 7 min and presents an ~200 km northward deviation of the obscuration maximum.

2.2. Ionosonde Records

The eclipse effects were studied by analyzing ionograms from the three ionosondes indicated in Table 1. Their locations are plotted as triangles in Figure 1. The ionosonde located at the Juan Soldado scientific

Table 1
List of Stations Used in the Present Work Ordered According to Geographic Latitude

Station	Geographic latitude	Geographic longitude	Solar apparent time	Geomagnetic latitude
Jicamarca (JI)	−12.0°	283.2°	UT-5.2	−0.6°
Tucumán (TU)	−26.9°	294.6°	UT-4.4	−15.5°
La Serena (LS)	−29.9°	288.7°	UT-4.8	−16.8°

Note. The geomagnetic coordinates are obtained from IGRF-13 for 2019 at 300 km altitude.

monitoring facility of Universidad de La Serena (LS, 29.9°S, 71.3°W) was within the path of totality. The station, deployed approximately 10 km north of the city of La Serena, Chile, is an IPS-42 ionosonde operated by the Centro Interuniversitario de Física de la Alta Atmósfera (Interuniversity Centre of Upper Atmosphere Physics, CInFAA in Spanish). On the day of the eclipse, 2 July 2019, the sampling interval of the IPS-42 ionosonde was every 5 min during the partial eclipse, every 20 s during the maximum obscuration, and every 15 min at other times. The details of this ionosonde, the new registration system used, and the new ionogram scaling software developed are explained in Appendix B.

The ionograms obtained at Tucumán (TU, 26.9°S, 65.4°W) and Jicamarca (JI, 12.0°S, 76.8°W) were analyzed using two ionogram scaling procedures: DISS (Appendix B) for TU and SAO-X (<https://ulcar.uml.edu/SAO-X/SAO-X.html>) for JI. The eclipse reached a maximum obscuration of 85% at TU and 52% at JI (90% and 56% obscuration, respectively, at 300 km altitude). The TU ionograms were recorded by the Low-Latitude Ionospheric Sensor Network (LISN, <http://lisn.igp.gob.pe/>), and the JI ionograms were recorded by the DIDbase (<https://ulcar.uml.edu/DIDBase/>). A correction was made for a 1 hr delay that was noticed in the TU ionograms when compared with other sensor measurements and their diurnal trends.

2.3. Total Electron Content

TEC was calculated using the program of Seemala & Valladares (2011, <http://seemala.blogspot.com/>) from Receiver Independent Exchange Format (RINEX) files. The software calculates the slant TEC (sTEC) from pseudorange measurements of each GNSS receiver. The clock errors and tropospheric effects are minimized using the phase and code values for the transmitted L1 and L2 GPS frequencies. Differential satellite biases and receiver bias are included in determining the absolute values of sTEC. In the calculation of vertical TEC (vTEC) from sTEC, the satellite elevation and azimuth angles are used. In this work, vTEC values corresponding to satellite elevation angles $\geq 15^\circ$ were selected to minimize possible errors.

The RINEX files were obtained from the Chilean network of GNSS receivers set up by the CSN, the International GNSS Service (IGS) network (Dow et al., 2009), the Argentine network (RAMSAC, Piñón et al., 2018), the Brazilian network (RBMC, www.ibge.gov.br), the Uruguayan network (REGNA, <ftp://pp.igm.gub.uy>), and the Colombian network (MAGNA, <https://geportal.igac.gov.co/>). These international networks of GNSS receivers enable the production of vTEC maps covering almost the entire South American continent with a high resolution (~500 stations) and temporal vTEC determinations every 30 s. The vTEC was computed for GNSS receivers at different geographic locations; these locations are graphically represented in Figure 1. Mean vTEC values were obtained from measurements localized to within $\pm 1^\circ$ latitude and $\pm 2^\circ$ longitude during a ± 2.5 min interval.

2.4. Model

The Sheffield University Plasmasphere Ionosphere Model (SUPIM; Bailey & Sellek, 1990; Bailey et al., 1993), namely, the version of Instituto Nacional de Pesquisas Espaciais (SUPIM-INPE; Bravo et al., 2017; Santos et al., 2016; Souza et al., 2010, 2013), was used to simulate the eclipse effects. SUPIM solves the time-dependent continuity, momentum, and energy balance equations along closed magnetic field lines for O^+ , H^+ , He^+ , N_2^+ , NO^+ , N^+ , and O_2^+ .

SUPIM-INPE incorporates the *E* region chemical reaction scheme from Huba et al. (2000), neutral densities from the NRLMSISE-00 model (Picone et al., 2002), and neutral winds from the HWM93 model (Hedin et al., 1996). In the model, the photoionization of neutral gases is calculated using the solar EUV fluxes from the EUVAC model (Richards et al., 1994), although the X-ray and Lyman- α fluxes are obtained from the SOLAR2000 model (Tobiska et al., 2000) covering wavelengths from 1.86 to 105 nm. In addition, the nighttime photoionization is calculated using nocturnal ionizing fluxes following Strobel et al. (1974) and Souza et al. (2010). According to Strobel et al. (1974), these fluxes are produced by resonantly scattered radiation with terrestrial and extraterrestrial sources. Such inputs have been used successfully in SUPIM-INPE, as confirmed by the results published by several studies (Bravo et al., 2017, 2019; Nogueira et al., 2013; Santos et al., 2016).

In the absence of an $E \times B$ vertical drift from the Jicamarca incoherent scatter radar (ISR) on the eclipse date, a composite vertical drift model was used (Bravo et al., 2017). This $E \times B$ vertical drift was deduced both from magnetometers (Anderson et al., 2004) between 07 and 17 LT and from the $E \times B$ vertical drift from the model of Fejer et al. (2008) for other hours. Specifically, the $E \times B$ vertical drift deduced from

magnetometers uses the difference between the magnetic field horizontal component of a magnetometer located at the magnetic equator, Huancayo (12.1°S, 75.3°W), and that of the magnetometer at Arequipa (16.5°S, 71.5°W) obtained from the INTERMAGNET site (www.intermagnet.org) and LISN, respectively. The $E \times B$ vertical drift from the model of Fejer et al. (2008) was multiplied by 0.5 for nighttime hours due to the overestimated simulations obtained during these hours.

The solar radiation input to the model was modified by the eclipse obscuration mask (*ObscMask*) obtained at 300 km altitude, as shown in Figure 1. Indeed, the radiation was calculated using a criterion similar to that published by Reinisch et al. (2018), which considers a decrease in solar EUV radiation during the eclipse; the coronal and chromospheric contributions reach 30% and 0%, respectively, at totality. Part of the coronal radiation remains to produce photoelectrons (Huba & Drob, 2017; Reinisch et al., 2018), and their contributions to photoionization are explained below. The modified radiation (I_R) for a given wavelength (λ) can be expressed as

$$I_R = I_{NT} + I_{RO}^{\lambda < 30.4} (1 - 0.7 \times ObscMask) + I_{RO}^{\lambda \geq 30.4} (1 - ObscMask), \quad (1)$$

where I_{NT} is the nighttime radiation. $I_{RO}^{\lambda < 30.4}$ and $I_{RO}^{\lambda \geq 30.4}$ are the ionizing radiations calculated by the EUVAC and SOLAR2000 models, as mentioned above, for $\lambda < 30.4$ nm (coronal range) and $\lambda \geq 30.4$ nm (chromospheric range), respectively. *ObscMask* is just a normalized value of the obscuration mask shown in Figure 1: *ObscMask* = 0 means that there is no eclipse, and *ObscMask* = 1 means eclipse totality. It is relevant to mention that the model was also run using zero coronal radiation at totality, that is, with only nighttime radiation at totality, and the results for *foF1* are not significantly different when compared with the results using nonzero coronal radiation. Since coronal radiation is responsible for only 2% of total photoionization (Reinisch et al., 2018), these results were already expected. Reinisch et al. (2018) pointed out that the energetic photoelectrons produced by coronal emissions are responsible for maintaining the ionization below 200 km during totality.

3. Results

3.1. Diurnal Variations in Ionospheric Characteristics

Figure 2 shows the manually scaled critical frequencies and virtual heights on 2 July 2019, the day of the eclipse. Definitions of all ionospheric characteristics are given in Table 2. Figures 3–5 show these characteristics for the interval from 17 to 23 UT (local afternoon) at stations LS, TU, and JI, respectively. The mean TEC and *hmF2* are also calculated for each station, together with the true height electron concentration profiles deduced from the ionograms. The shaded intervals represent the eclipse partial and total shadowing times computed at 300 km altitude.

At LS (Figure 3), which is within the total obscuration path, there is a clear decrease in *foF1* and *foE*, as shown during previous eclipses (e.g., Cheng et al., 1992). The virtual heights *h'F* and *h'E* also show low values at times during the eclipse. As the eclipse occurred near sunset, the *F1* and *E* layers would have been affected by nighttime ionospheric recombination. On the other hand, *foF2* does not decrease during the initial stages of the eclipse; *foF2* does show a dip at totality but increases after the maximum occultation. The *foF1*, *foE*, *h'F2*, and *h'E* parameters were observed throughout the eclipse at JI but only before the maximum occultation at LS and TU: The LS and TU parameters disappear before the maximum occultation time as solar radiation decreases during sunset. As in previous eclipses, *foF2* and *h'F* reach minima several minutes after the maximum occultation. Unlike in some other eclipses (e.g., Reinisch et al., 2018), *hmF2* has a local minimum rather than a maximum near totality.

The *ftEs-fbEs* and *h'Es* values correspond to a high/low/flat-type sporadic *E* layer sequence with a rather high *fbEs*. Though highly variable, *ftEs-fbEs* and *h'Es* are not outside of the expected levels for any significant time during the eclipse. The sharp decrease in *ftEs-fbEs* near totality is definitely due to an *f*-type *Es* and results from the combined effect of a reduction in *ftEs* and an increase in *fbEs*. The presence of this kind of sporadic *E* layer may not be associated with the eclipse since this behavior is present on the following days at the same local times. The sudden jump in *h'Es* before totality is caused by the transition from an *h*-type *Es* to an *l*-type *Es*, the latter having a larger top frequency. The estimated peak height of the maximum electron concentration (*hmF2*) shows little variation at the beginning of the eclipse, followed by a sudden drop just

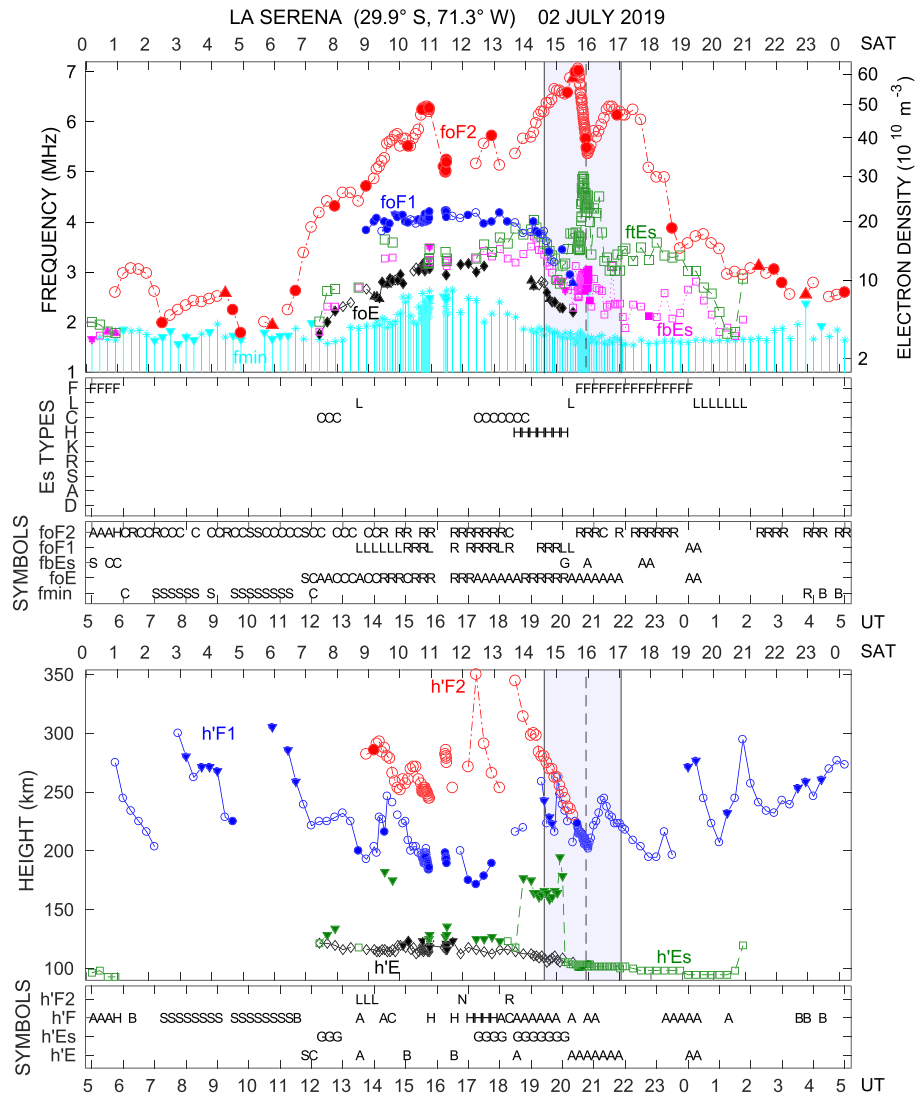


Figure 2. Diurnal variations of $foF2$, $foF1$, foE , $ftEs$, $fbEs$, and $fmin$ (top panel), observed types of the sporadic E layer (second panel from top), and associated descriptive letters (third panel) at La Serena ($29.9^{\circ}S$, $71.3^{\circ}W$) on the day of the eclipse (2 July 2019). Unqualified values (open symbols), values qualified as doubtful (filled symbols), and values lower than and higher than the indicated value (filled triangles, upward, and downward, respectively). Same for $h'F2$, $h'F1/F$, $h'E$, and $h'Es$ (fourth and fifth panels). Eclipse onset, totality and eclipse end (shaded interval). Rules to qualify and to describe values are those given by Piggott and Rawer (1972).

before eclipse totality and a later increase to larger values than before the eclipse. The corresponding $N(h)$ shows a reduced F layer width near totality, coinciding with a decrease in $foF2$. There is an apparent electron concentration decrease at altitudes between 100 and 250 km from the beginning of the eclipse up to approximately half an hour after totality.

The eclipse effects observed at TU (Figure 4) are more extensive than and different from those noted at LS. The TU foE and $foF1$ show more significant decreases than those at LS, beginning with the arrival of the moon shadow at TU. While $foF2$ similarly decreases near totality, there is a substantial increase in the TU $foF2$, followed by a decrease a few minutes after the maximum obscuration. The TU $foF2$ and virtual heights ($h'F2$ and $h'F1/F$) also show oscillations following the maximum obscuration. The sudden jump in $h'E$ minutes before the arrival of the shadow is mainly associated with the presence of an l -type sporadic E layer that impacted the ionogram reduction. The TU $hmF2$ shows a decreasing wave-like trend from the beginning of the eclipse and also presents a sudden increase before the end of the eclipse. As at LS, the $N(h)$ profile indicates evident electron concentration depletion between 100 and 200 km at the beginning of the event. No F

Table 2
Ionospheric Characteristics From Ionograms

Ionospheric characteristic	Abbreviation
Critical frequency $F2$ layer	f_oF2
Peak electron density height $F2$ layer	$hmF2$
Virtual height $F2$ layer	$h'F2$
Critical frequency $F1$ layer	f_oF1
Virtual height $F1$ layer	$h'F1$
Critical frequency E layer	f_oE
Virtual height E layer	$h'E$
Top frequency E_s layer	f_tE_s
Virtual height E_s layer	$h'E_s$
E_s blanketing frequency	f_bE_s
Type of E_s	E_s type
Minimum frequency	f_{min}
Transmission factor	M3000

region thinning is shown near totality. In contrast, the width is almost constant, and $NmF2$ reaches a maximum at totality. Moreover, $hmF2$ and the F region width exhibit maxima before the eclipse and then oscillate after the end of the eclipse. These F region changes do not seem to be caused by the eclipse itself but are related to transport and internal plasma behavior.

The ionospheric virtual heights and top E_s frequencies at JI (Figure 5) generally show values within the observed variability, indicating that for this location, with only a partial eclipse, the eclipse exhibits smaller impacts. There is a systematic reduction in f_oF1 , f_oE , and f_tE_s at the onset of the eclipse, while the f_oF2 minimum occurs after the maximum obscuration, as expected. Unlike that at LS and TU, the JI f_oE is observed throughout the eclipse and disappears only near sunset. At JI, f_oF1 increases after the maximum obscuration until the $F1$ layer disappears. The F region maximum concentration slowly increases, and its height decreases. This

behavior does not seem to be related to changes in the solar zenith angle. The electron concentrations at lower altitudes (between 100 and 250 km) show a clear reduction, as was noted for LS and TU. These reductions are related to the decrease in solar radiation during the eclipse.

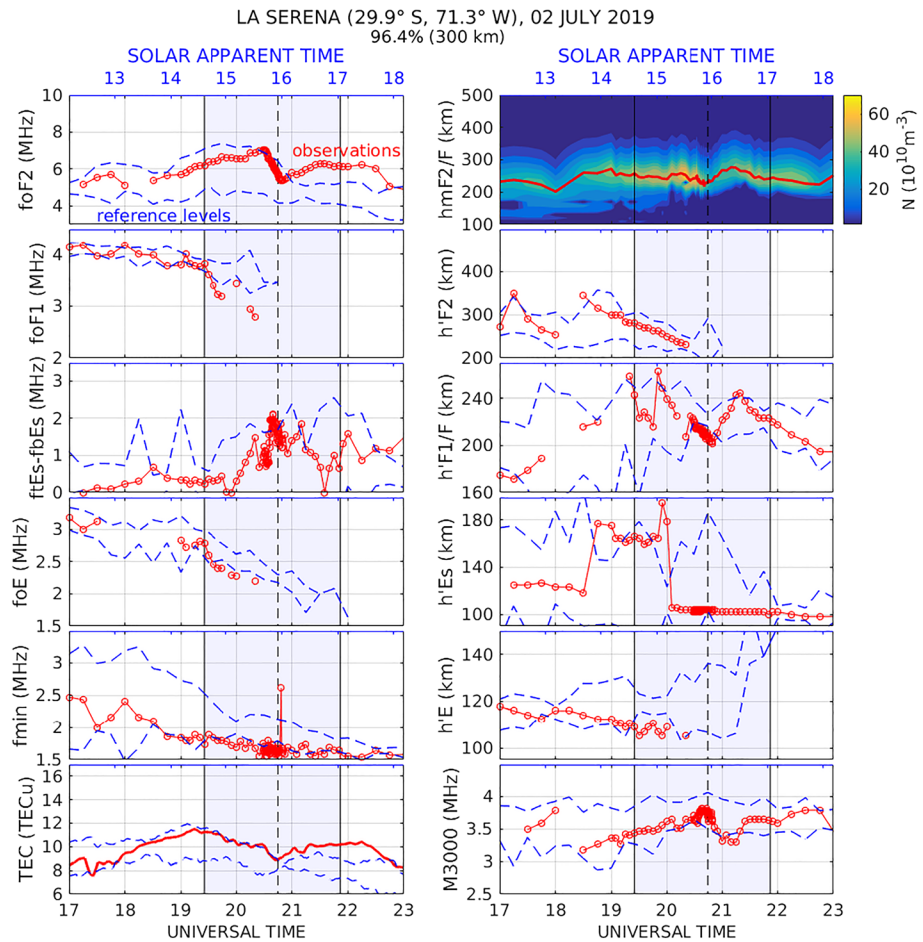


Figure 3. Critical frequencies (f_oF2 , f_oF1 , f_oE , and $f_tE_s-f_bE_s$), virtual heights ($h'F2$, $h'F1/F$, $h'E$, and $h'E_s$), real heights ($hmF2/F$, shown together with vertical distribution of the electron concentration), f_{min} , M3000, and TEC during the eclipse (2 July 2019) at La Serena (29.9°S, 71.3°W). Observed values (circles and continuous red lines). Calculated median \pm interquartile range for 15 geomagnetically quiet days ($K_p \leq 2^+$) between 29 June and 20 July 2019 (blue dashed lines). Eclipse onset, maximum obscuration, and eclipse end (shaded interval).

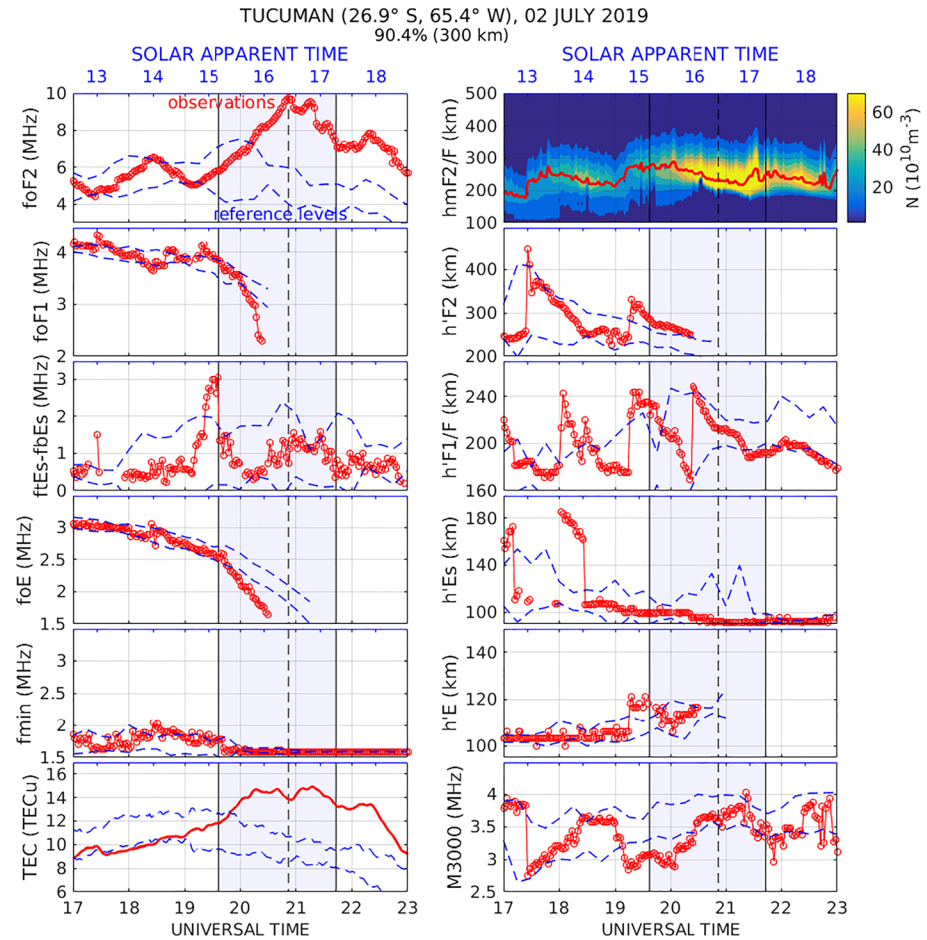


Figure 4. Critical frequencies ($foF2$, $foF1$, foE , and $fEs-fbEs$), virtual heights ($h'F2$, $h'F1/F$, $h'E$, and $h'Es$), real heights ($hmF2/F$, shown together with vertical distribution of the electron concentration), $fmin$, M3000, and TEC during the eclipse (2 July 2019) at Tucumán (26.9°S, 65.2°W). Observed values (circles and continuous red lines). Calculated median \pm interquartile range for 15 geomagnetically quiet days ($Kp \leq 2^+$) between 29 June and 20 July 2019 (blue dashed lines). Eclipse onset, maximum obscuration, and eclipse end (shaded interval).

The variability of $fmin$ and M3000 was also determined for LS, TU, and JI (Figures 3–5). The LS $fmin$ is generally lower than expected before, during, and after the eclipse. There is a single $fmin$ outlier related to an ionosonde failure, and the values during the eclipse time interval steadily decrease at a linear rate of 0.13 MHz/hr, as expected from the reduction in solar-associated radio wave absorption. No significant association with the eclipse can be observed. In the case of TU, which is 6° east and 3° north of LS, $fmin$ is usually observed at nighttime; similarly, no-eclipse effect is found. At JI, which is approximately 6° west and 18° north of LS, $fmin$ is well within the expected variability, which is rather small (less than 0.5 MHz), during and after the eclipse. The rate of decrease is approximately 0.04 MHz/h during the eclipse interval. The much-reduced rate of decrease is consistent with JI, slightly west and much north of LS.

M3000 is related to the width of the ionospheric layer. A small value corresponds to a thick ionospheric layer, while larger values correspond to a slim layer. At LS, M3000 is within the expected variability before, during, and after the eclipse; however, there is a clear symmetric peak, approximately 20 min wide, centered at totality. This small peak (0.25 MHz) coincides with the $foF2$, $hmF2$, $h'F1/F$, and TEC minima, suggesting a change in the shape of the $N(h)$ distribution in addition to changes in the other characteristics mentioned above. By contrast, the longer double-humped M3000 peak centered on the maximum obscuration observed at TU is similar to the $foF2$ and TEC peaks. The secondary M3000 minima at TU coincide with the TEC minima but occur tens of minutes before the $foF2$ minima. Moreover, no such feature is observed for $hmF2$ and $h'F1/F$. The relevance of this result is not yet clear. In the case of JI, M3000 is rather low

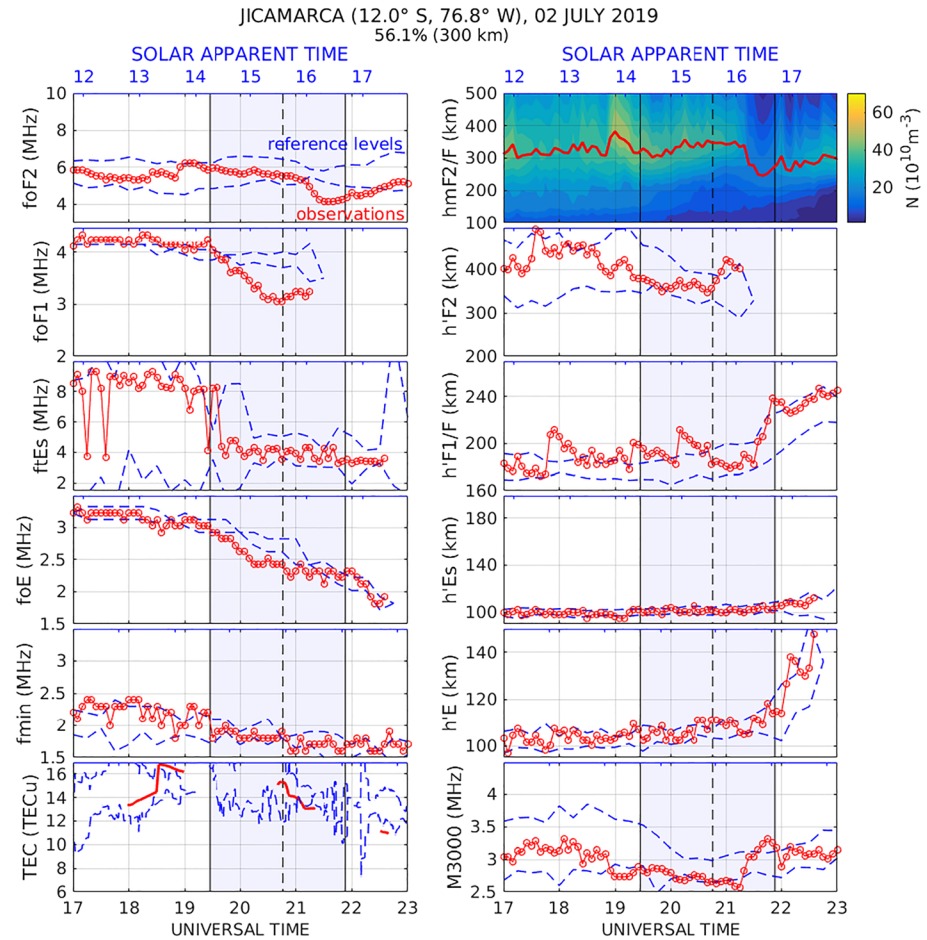


Figure 5. Critical frequencies ($foF2$, $foF1$, foE , and fEs), virtual heights ($h'F2$, $h'F1/F$, $h'E$, and $h'Es$), real heights ($hmF2/F$, shown together with vertical distribution of the electron concentration), $fmin$, M3000, and TEC during the eclipse (2 July 2019) at Jicamarca (12.0°S, 76.8°W). Observed values (circles and continuous red lines). Calculated median \pm interquartile range for 15 geomagnetically quiet days ($Kp \leq 2^+$) between 29 June and 20 July 2019 (blue dashed lines). Eclipse onset, maximum obscuration and eclipse end (shaded interval).

during the ± 45 min interval centered on the maximum obscuration. No significant association is found with the variations in $foF2$, $hmF2$, $h'F1/F$, or $hmF2$.

TEC presents much more significant variations at TU and JI, as shown in Figures 4 and 5, respectively. Particularly sparse values are found at JI due to a lack of correct measurements. Even so, the TEC values obtained at JI are as expected, indicating a minimal impact at locations with only partial eclipse obscuration. A substantial increase in TEC at TU is shown in Figure 4 from the beginning of the partial eclipse. The TEC values obtained are much larger than expected during and after the eclipse time. This large increase in the electron concentration seems to be associated with the increment in $foF2$, suggesting ionization of the F2 layer probably related to plasma transport at these altitudes.

3.2. Latitude-Time Variations in TEC

The mean TEC computed along the La Serena geographic meridian for latitudes between 20°N to 60°S is shown in Figure 6 (left; the right side of Figure 6 will be discussed in section 3.3). The contours of this figure represent the eclipse obscuration mask calculated at 300 km altitude, while the latitudes corresponding to the magnetic equator and the average EIA crests are denoted with continuous and dashed horizontal lines, respectively.

This figure shows a clear TEC reduction at latitudes from approximately 40°S to 30°S and an increase at latitudes to the north during the eclipse time interval (19.17 to 21.77 UT). This is also observed for $foF2$ in

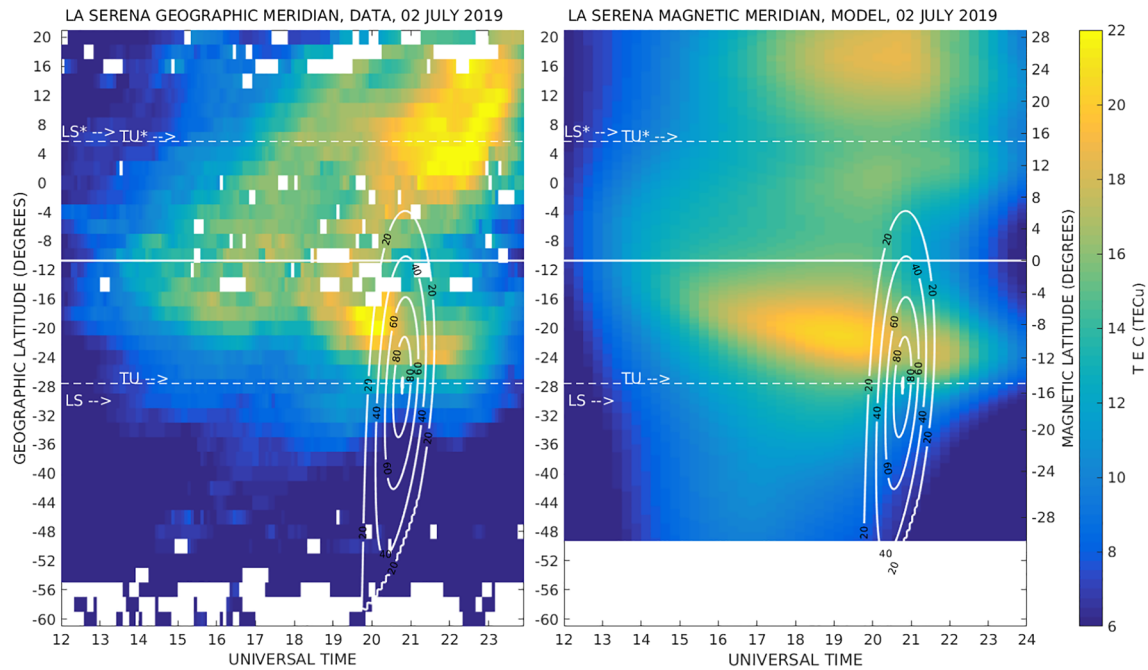


Figure 6. Latitude-time TEC distribution along the La Serena (LS: 29.9°S, 71.3°W) geographic meridian (observations, left) and geomagnetic meridian (SUPIM-INPE model, right). The eclipse path and its interval are highlighted with white contours, representing the latitudinal sections and the corresponding times with 20%, 40%, 60%, 80%, and 100% eclipse obscuration at 300 km altitude. Magnetic equator (horizontal continuous line). Geomagnetic latitudes $\pm 15^\circ$ (horizontal dashed lines). La Serena (LS), Tucumán (TU: 26.9°S, 65.2°W), and corresponding geomagnetic conjugate latitudes (arrows).

Figures 3 and 4. Nevertheless, large variabilities are also found at these latitudes before the eclipse onset time. An increase in TEC is found at latitudes between approximately 0°N and 12°N during the eclipse period. These latitudes correspond to magnetically conjugate regions to the eclipse path (LS* is $\sim 7^\circ\text{N}$, and TU* is $\sim 6^\circ\text{N}$) and therefore may be affected by eclipse-induced disturbances, as suggested by Le, Liu, Yue, and Wan (2009). The reduction in TEC at LS during the eclipse time is also shown in Figure 3. The minimum TEC value is found at (and corresponds to) the time of totality.

3.3. Model Diurnal and Latitude-Time Variations

The diurnal variations of $foF2$, $hmF2$, $foF1$, foE , and TEC are simulated. Note that $foF1$ is derived from the simulated $N(h)$ distribution at 190 km altitude, the usual height for the F1 layer, since no true secondary maximum is evident. Figure 7 shows some of the diurnal variations of $foF2$, $hmF2$, and TEC during the eclipse at JI, TU, and LS. The results for foE and $foF1$ are discussed in sections 4.1 and 4.2.

The responses obtained by SUPIM-INPE fit well with the JI observations. The good correlation in $hmF2$ between the observations and simulated responses suggests that the composite drift from the model and the magnetometer-deduced drift is adequate for the hours without an eclipse. As JI is located at an equatorial latitude, its height is affected by vertical drift but not by thermospheric winds. Therefore, the match between the JI simulation and measurements indicates the selection of a correct drift parameter. For TU and LS, the simulated responses show agreement with regard to the daytime increases and average values of parameters. Nevertheless, there are substantial differences in the daytime $foF2$ and much less variability in the $hmF2$ simulations. These differences could be related to changes in the wind direction or the presence of waves not considered in this simulation.

During the eclipse time, the differences between the typical condition simulation (blue lines) and the eclipse condition simulation (green lines) show a small decrease in $foF2$ and a slight increase in $hmF2$, which are not enough to reproduce the observations. Furthermore, during the eclipse at JI, there is an increase in the observed $hmF2$, following a decrease in $foF2$. By contrast, there is an increase in $foF2$ at both TU and LS. All these results suggest the existence of a prereversal enhancement (PRE) in the $E \times B$ vertical drift (Eccles et al., 2015). For this reason, a centered PRE has been added during the eclipse over the previous

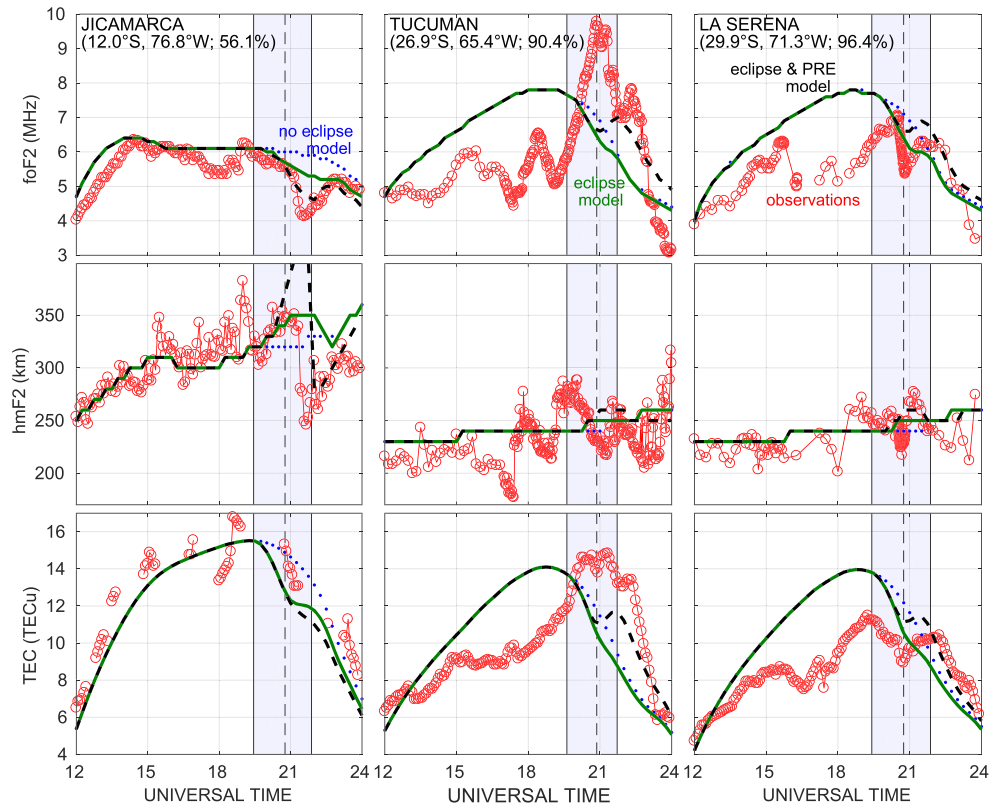


Figure 7. SUPIM-INPE simulations of $foF2$, $hmF2$, and TEC during the 2 July 2019 eclipse for Jicamarca (12.0°S , 76.8°W), Tucumán (26.9°S , 65.2°W), and La Serena (29.9°S , 71.3°W). Without the hypothetical prereversal electric field (green solid lines), with the PRE (black dashed lines), under no-eclipse geomagnetically quiet conditions (dotted blue lines), and observations (open circles). Eclipse onset, maximum obscuration, and eclipse end (shaded interval).

input $E \times B$ drift of SUPIM-INPE. The simulations with the added PRE drift are shown with black lines in Figure 7. The results with this drift show better agreement with the observations during the eclipse time. The simulated $foF2$ and $hmF2$ now reproduce the observations at JI. At LS, $foF2$ and TEC increase to a secondary maximum after totality and then decrease, reproducing the observations fairly well. Similar $foF2$ and TEC variations are modeled at TU; however, the modeled parameters at totality are minima, while the observed parameters are maxima, and the observed secondary maxima lag the modeled ones by approximately 1 hr. Moreover, the model does not reproduce the observed $foF2$ at TU and LS during several hours before the eclipse. These issues are related to the large day-to-day variability of $foF2$ and TEC, as discussed in the following section.

The SUPIM-INPE-computed TEC along the LS geomagnetic meridian at geomagnetic latitudes between approximately 28° and -30° (geographic latitudes 20°N and 49°S) is shown in Figure 6 (right). The simulated and observed (left) TEC can be compared directly because the geographic and geomagnetic meridians almost coincide at LS (the geomagnetic declination at LS is -0.01°). The geomagnetic meridian is a few degrees east of north for latitudes south of LS and a few degrees west of north for latitudes north of LS. The simulated TEC clearly shows the development of the EIA in the Southern Hemisphere. The TEC latitudinal maximum increases with time and moves southward between approximately 14 and 18 UT (~ 09 and 13 SAT) at geomagnetic latitudes from -16° to -21° . The maximum TEC decreases after 18 UT, as expected during the local afternoon. A superimposed TEC dip is evident during the eclipse. However, the movement of the TEC latitudinal maximum does not seem to change at the same times. The modeled EIA and superimposed eclipse changes fairly reproduce the observed changes. The largest differences between the simulated and observed TEC are found before the eclipse for several hours centered at approximately 18 UT and range over geomagnetic latitudes from -18° to -32° . This is consistent with the already noted differences between the simulated and observed $foF2$ and TEC at JI and LS (Figure 7).

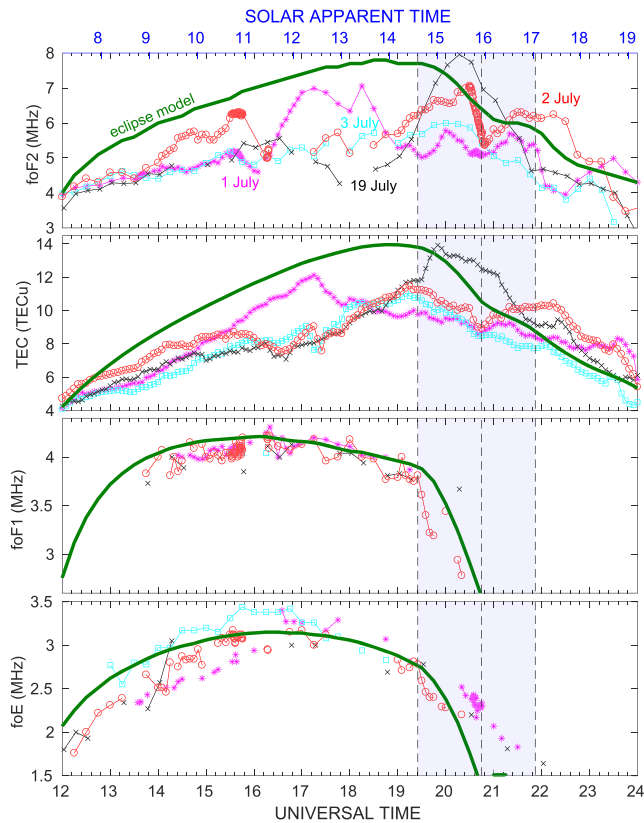


Figure 8. SUPIM-INPE simulations of $foF2$, $foF1$, foE , and TEC without the prereversal electric field during the 2 July 2019 eclipse (solid green line) at La Serena (29.9°S, 71.3°W) and observations on 1 (stars), 2 (open circles), 3 (open squares), and 19 July 2019 (crosses).

such as the 1986 eclipse reported by Cheng et al. (1992). The same feature is also revealed in the measurements and models for the Great American Eclipse of 2017 by Reinisch et al. (2018).

$F1$ layer stratification is seen at TU and LS during the first minutes of the eclipse, but it is difficult to determine whether this stratification is connected to the event or a regional (low-latitude) behavior. This stratification is consistent with that observed in some other eclipses, the so-called eclipse $F1.5$ layer, which is generated by a faster recovery time at lower altitudes and produces an inflection of the concentration profile (Rishbeth, 1968).

The existence of a sporadic E layer and its blanketing behavior are evident in Figures 3–5. The decreases in the LS and TU $ftEs$ - $fbEs$ during the initial and final parts of the eclipse indicate blanketing during these periods. During the responses of the equatorial eclipses of 1987 and 1999, there was also a blanketing E layer, which intensified during the eclipses (Chandra et al., 2007; Cheng et al., 1992; Sridharan et al., 2002). During this eclipse, the $ftEs$ - $fbEs$ value reaches a maximum near totality at LS and TU, indicating a sizeable sporadic E layer occurring during this period, but the blanketing behavior is not observed. At JI, far from the totality path, only the $ftEs$ parameter is shown because there is no blanketing. The behavior of the sporadic E layer at JI is opposite to the behavior noted at the other stations, showing a reduction in occurrence several minutes after the onset of the eclipse. This finding supports the idea that the sporadic E layer at LS and TU is associated with the eclipse, possibly generated by a gravity wave (GW) along the path of totality (Chen, Zhao, Zhang, et al., 2011).

The $foF2$ at JI shows an apparent decrease during the maximum obscuration, as does $hmF2$. These decreases lead to a TEC reduction and an overall lowering of the layer. However, at TU, a substantial TEC increase is detected due to an increase in $foF2$ but with a slight and almost constant decrease in $hmF2$. The electron concentration increase at TU should not be related to northward or southward winds because the altitude of the

4. Discussion

4.1. Reference Quiet Day Selections

Figure 8 shows a plot of the $foF2$, TEC, $foF1$, and foE at LS for 4 days (1, 2, 3, and 19 July). Despite being magnetically very quiet, these days confirm that there is considerable $foF2$ and TEC variability, as expected for equatorial and low latitudes, where electrodynamic processes are paramount (e.g., Kelley, 2009). In particular, $foF2$ and TEC are larger on 19 July than on the day of the eclipse, almost from the onset of the eclipse to halfway between totality and the end of the eclipse. The opposite is found on 1 and 3 July. Many published papers have made single quiet day comparisons (e.g., Amabayo et al., 2014; Momani et al., 2010) and may have overestimated or underestimated the ionospheric response to the moon shadow. To avoid this ambiguity, Reinisch et al. (2018) compared observed eclipse variations with model variations instead.

By contrast, $foF1$ and foE are less variable during several hours before the eclipse on quiet days. Unfortunately, no variability can be assessed during most of the eclipse interval since both the $F1$ layer and the E layer disappear near sunset.

4.2. Ionospheric Impacts in Different Layers

Figures 3–5 (for LS, TU, and JI, respectively) show reductions in the E and $F1$ layer electron concentrations following the start of the eclipse, as these layer electron concentrations are mainly dependent on the production and loss of ionization (Rishbeth, 1968).

The foE and $foF1$ frequencies measured near the totality path (LS and TU) disappear before the maximum obscuration, but those at JI do not vanish and instead show an increase after the maximum obscuration. This direct dependence of the E and $F1$ layer critical frequencies on solar radiation shows similarities to measurements of previous eclipses at low latitudes,

maximum layer neither increases nor decreases. This remarkable response difference at almost identical low latitudes highlights the large variabilities found over low latitudes. At equatorial latitudes, the $JI\ foF2$ significantly decreases ~ 30 min after the maximum obscuration, resulting in a subsequent reduction in $hmF2$. The local minima at JI , TU , and LS are delayed relative to the maximum obscuration by 40, 62, and 4 min, respectively. These delays do not follow an expected sequential latitudinal response, suggesting that combined processes are at work, not just shadow effects. The highly variable $F2$ layer response to the eclipse is consistent with theoretical expectations (Rishbeth, 1968) that consider plasma transport and thermal processes. Such variability was also observed during several eclipses (see Adekoya et al., 2015; Chandra et al., 2007; Chen, Zhao, Ning, et al., 2011; Cheng et al., 1992; Chukwuma & Adekoya, 2016; Le, Liu, Yue, Wan, & Ning, 2009; Sridharan et al., 2002).

4.3. Ionospheric Model for Southern Latitudes

The SUPIM-INPE model has been found to provide the most accurate simulation representation of low-latitude ionospheric effects over South America (Bravo et al., 2017, 2019; Santos et al., 2016; Souza et al., 2010, 2013).

Figure 7 shows the observed and SUPIM-INPE-simulated $foF2$, $hmF2$, and TEC variations with and without the eclipse obscuration. The model does not effectively reproduce the observed $foF2$ dip after the maximum obscuration at JI , the significant increases in the $TU\ foF2$ and TEC, or the decreases in the $LS\ foF2$ and TEC during totality and the subsequent increase and peak at the end of the eclipse. The model produces only small decreases in the TU and $LS\ foF2$ and TEC in response to the eclipse, giving the most significant reductions during the maximum obscuration. However, when an artificial PRE is added to the drift, the simulations better reproduce the observations at JI . This modeling result is consistent with a PRE related to a more substantial fountain effect, increasing the height and decreasing the electronic concentration at equatorial stations and bringing plasma to low latitudes. A similar PRE has been observed before (Adekoya et al., 2015; Chen, Zhao, Ning, et al., 2011) coincident with the appearance of the $F3$ layer in the JI ionogram rising between 21.25 and 21.58 UT (see <http://ulcar.uml.edu/DIDBase>). Finally, the observed $foF1$ and foE (Figure 8) are found to be in reasonable agreement with the model results up to the approximate time of maximum obscuration. No further firm comparison can be made after the maximum obscuration, however. Both the measurements and the simulated values sharply decrease before the maximum obscuration. The simulations with model radiation input using all wavelengths for $foF1$ and foE do not differ significantly from the results that use only coronal radiation.

The true height profiles provide a truer indication of the reduced electron concentration than the reduction determined from only critical frequency variations (Beynon, 1955). Figure 9 shows the plasma frequency height distribution along the LS meridian at 21 UT under both no-eclipse and eclipse conditions. The plasma frequency differences between the two conditions can be negative or positive for geomagnetic southern latitudes depending on the altitude. A reduction in plasma frequency is found at all latitudes along the eclipse path at altitudes between 150 and 300 km. This reduction agrees with observations of more substantial effects in the E and $F1$ layers than in the $F2$ layer. The opposite effect is shown at higher altitudes (between 350 and 500 km), where the frequency is increased only at the latitudes along the totality path.

The increased electron concentration may suggest plasma diffusion or transport through magnetic field lines that occur at low latitudes, which increases the $F2$ layer concentration, while the reduced radiation during the eclipse lowers the electron concentration contents of the E and $F1$ layers. No similar results for low latitudes seem to have been reported for previous eclipses at southern or northern latitudes using ISR (e.g., Cherniak & Lysenko, 2013; Goncharenko et al., 2018; Salah et al., 1986), although most ISR facilities are located the mid- and high latitudes of the Northern Hemisphere.

The plasma frequency height distribution changes with time over LS under both no-eclipse and eclipse conditions, as shown in Figure 9. The plasma frequency differences associated with the eclipse are negative at lower altitudes, and the plasma frequency reduction coincides with a broad $hmF2$ maximum just after totality. Furthermore, the simultaneous positive difference maximum at high altitude moves downward even after the eclipse ends.

Ultimately, the simulated and observed plasma frequency changes with time are fairly consistent.

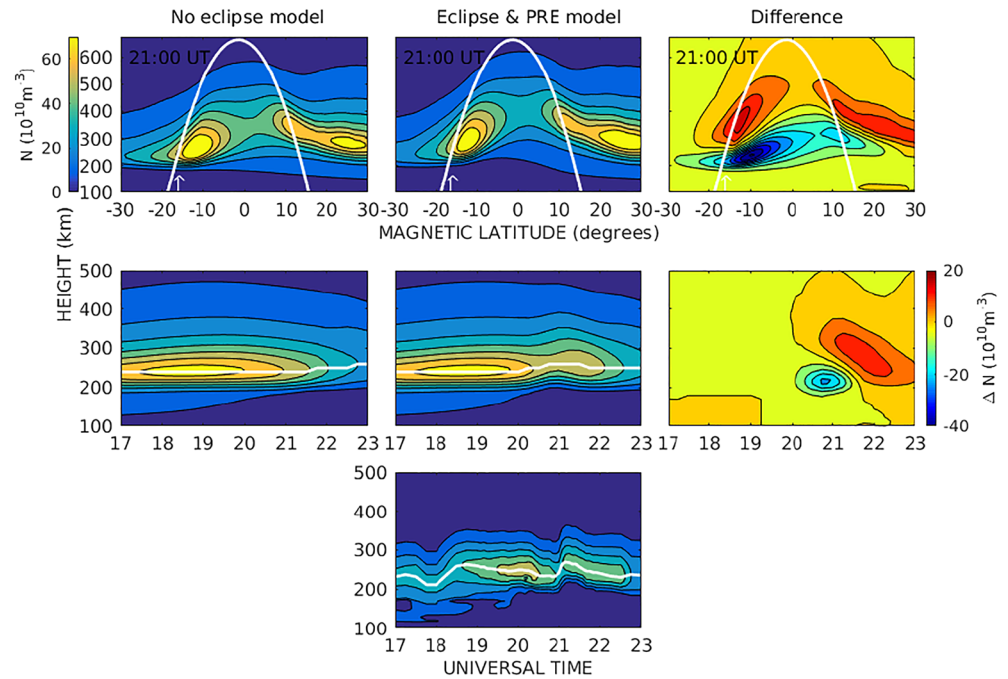


Figure 9. SUPIM-INPE simulations of the height-latitude distribution plasma frequency (top panel) along the La Serena (29.9°S, 71.3°W) magnetic meridian (~1°E) for the 2 July 2019 eclipse at 21 UT and height-time simulations (middle panel) over La Serena. No-eclipse geomagnetically quiet conditions (left). With the hypothetical prereversal enhancement (middle). Differences between the eclipse and geomagnetically quiet conditions (right). Height-time distribution of the observed plasma frequency (bottom). La Serena magnetic latitude is indicated with arrows.

4.4. Magnetically Conjugate Latitudes

The SUPIM-INPE model estimations for the northern latitudes along the LS magnetic meridian can also be discussed using Figure 9. While decreases in the maximum electron concentration are observed along the eclipse totality path at 200–300 km, increased concentrations are simulated over the conjugate latitudes with a maximum at 300–400 km. This effect is consistent with an increase in TEC, as shown in Figure 6. At the LS conjugate location (17°N magnetic latitude), an increased concentration is found at an altitude of 400 km but moves to lower altitudes at higher latitudes. This change in the altitude of the maximum concentration increase with latitude suggests that the conjugate effect of the eclipse is also affected by the EIA and the fountain effect. These increases and altitudes are in agreement with previous observations and models of TEC at conjugate locations during eclipses (He et al., 2018; Huba & Drob, 2017; Le, Liu, Yue, Wan, & Ning, 2009; Sergeenko, 2018). In particular, the model of Huba and Drob (2017) suggests that these effects can be explained by a change in conductivity derived from the reduced solar radiation in the area of obscuration, leading to a modification of the electrostatic potential that is being reflected through field lines in the opposite hemisphere. However, the latitude-time TEC plots for the other quiet days (not shown) also show high TEC at these hours in the conjugate region. In addition, manually checked automatic scalings of the ionograms for locations closer to conjugate latitudes (Boa Vista, 2.8°N, 60.7°W; Ramey, 18.5°N, 67.1°W) do not show significant f_oF2 differences during the eclipse time (<http://giro.uml.edu/didbase/scaled.php>). These observations seem to be more attributable to the fountain effect.

5. Conclusions

The ionospheric response to the total solar eclipse on 2 July 2019 is presented using observations from one ionosonde in La Serena (LS: 29.9°S, 71.3°W) located along the path of totality. Data from ionosondes located at Tucumán (TU: 26.9°S, 65.4°W) and Jicamarca (JI: 12.0°S, 76.8°W), with 85% and 52% obscuration (90% and 56%, respectively, at 300 km altitude), respectively, are employed for comparison. High spatial and temporal resolution determinations of TEC over almost the entire South American continent are also

considered. Furthermore, the impact of the eclipse on the ionosphere is simulated using SUPIM-INPE to provide a regional representation at low latitudes.

Although the eclipse occurred within an extended geomagnetically quiet period, the $F2$ layer characteristics and TEC show considerable variability, which is expected for equatorial and low latitudes. Overestimates or underestimates of the ionospheric response to the moon shadow are likely when single quiet day observations are used for comparison at low latitudes.

The eclipse effects at LS and TU are significantly different, even though the two locations are within 1° geomagnetic latitude and are separated by less than an hour of local time. It is believed that this result is associated with the variability of the EIA.

Below 200 km, the foE and $foF1$ at LS, TU, and JI decrease with the magnitude of obscuration, as expected. $F1$ layer stratification is observed at TU and LS during the first few minutes of the eclipse shadow, but it is difficult to determine if the origin of this stratification is connected to the eclipse.

The sporadic occurrence of the E layer at JI is opposite to that at LS and TU. There is an apparent reduction several minutes after the onset of the eclipse, which suggests that the LS and TU sporadic E layers may be associated with a GW (Chen, Zhao, Zhang, et al., 2011).

Different responses of the $F2$ layer are expected at JI relative to LS and TU (equatorial vs. low latitudes). On the other hand, given their close proximity, the difference in the behavior between LS and TU is remarkable. At LS, $foF2$ decreases near totality, while $hmF2$ has a peak ~ 30 min after totality. In contrast to those at LS, the TU $foF2$ increases significantly after the onset of the eclipse, and $hmF2$ steadily decreases until ~ 62 min after the maximum obscuration. At JI, $foF2$ steadily decreases after onset and then decreases more sharply beginning ~ 40 min after the maximum obscuration until ~ 30 min later, when a decrease in $foF2$ is accompanied by a rapid fall in $hmF2$. The calculations of Reinisch et al. (2018) indicate that $hmF2$ should increase as photoionization decreases below the $F2$ layer peak. Thus, F layer effects may result from some combined processes, not just from solar shadow forcing.

The SUPIM-INPE-simulated $foF2$, $hmF2$, and TEC effectively reproduce the observations at JI several hours before the eclipse, but $foF2$ and TEC are overestimated at LS, particularly those at TU. Nevertheless, these overestimations are within the large day-to-day variability found for several days centered on the day of the eclipse. The initial modeling during the eclipse is not that good. When an artificial prereversal enhancement (PRE) is added to the input drift, the simulations better reproduce the observations at JI, are qualitatively better for LS, and are out of phase for TU up to the end of the eclipse. This PRE has been observed previously by other researchers and coincides with the occurrence of the $F3$ layer at JI between 21.25 and 21.58 UT.

The SUPIM-INPE TEC increases calculated at the eclipse conjugate locations in the Northern Hemisphere confirm previously published results. It was suggested that these increases are associated with conductivity changes due to the reduced solar radiation during the obscuration. The generated electrostatic potential modification would propagate through magnetic field lines to the opposite hemisphere. However, the observations seem to be more attributable to the fountain effect.

Appendix A: Historical Perspective

Ratcliffe (1956) produced a survey of solar eclipses and the ionosphere by considering 200 events from 1920 (even before the ionosphere was experimentally discovered) to 1955. This survey includes work on early radio observations, which demonstrated that solar radiation rather than corpuscular ionization was the primary cause of ionization production (Mitra et al., 1933; Wireless World, 1932). Additionally, different impacts on density variations and plasma transport are produced in the different ionospheric layers (Higgs, 1942).

Earlier radio wave absorption measurements (Palmer riometers, 61.7°N , 149.2°W) and height distributions of electron concentration observations (from the Millstone Hill ionosonde and ISR 42.6°N , 71.5°W) during the Alaskan 20 July 1963 eclipse were reported by Lerbald et al. (1965) and Evans (1965a), respectively. In the radio wave absorption case, the measurements showed unexpected recombination and attachment behaviors, and the authors called for an interpretation. At Millstone Hill, TEC decreases and initial F region maximum electron concentration increases were associated with the cooling and downward movement of the F

region. Evans (1965b) revisited the Alaskan 20 July 1963 eclipse and surveyed the effects of 10 eclipses during 1935–1961, showing that $foF2$ increases are rare and are more likely to occur at locations with a large geomagnetic inclination. Some models of the effects of solar eclipses on the ionosphere were produced during the 1960s (De Jager & Gledhill, 1963) in an attempt to interpret the enhancement of the $F1$ cusp and the appearance of other stratifications (e.g., the $F1.5$ layer). Furthermore, with the study of the impacts of different eclipses, it was possible to determine the recombination coefficients of ionospheric species (Bates & McDowell, 1957), the identical radiation origin responsible for the production of both the $F1$ layer and the $F2$ layer (Szendrei & McElhinny, 1956), and the existence of different types of molecular ions in the E layer (Bates & McDowell, 1957; Bowhill, 1961; Rishbeth, 1968). Moreover, the ionospheric theory during solar eclipses was systematized (Rishbeth, 1968; Rishbeth & Garriot, 1969).

During the following decades (1960–2015), hundreds of papers dealing with specific ionospheric effects during single events and series of eclipses were published. A simple review of the terms and the most meaningful stories are given by Mansoori et al. (2011).

Using a combination of vertical soundings, a very low-frequency radio wave propagation receiver, and differential Doppler radar observations during the 23 September 1987 eclipse, Cheng et al. (1992) were able to establish the following: (a) while the $F1$ layer was controlled by local solar radiation, the $F2$ layer was controlled by radiation at the equator (via the equatorial ionospheric anomaly, EIA); (b) the D region reacted to the decreased solar radiation with an 8 min delay; and (c) there was evidence that an acoustic gravity wave (AGW) was produced with a 17–23 min period and 293 km wavelength.

With the advent of vast and large arrays of GNSS receivers (which measure the multiple frequency transmissions of restricted satellite beacons), it was possible to obtain the full effects of solar eclipses on the TEC. Afraimovich et al. (2002) determined TEC decreases of 0.2–0.3 TECu, a time delay relative to totality of approximately 4 min, and both $foF2$ decreases and $hmF2$ increases using 70 European GPS stations and the Chilton ionosonde (51.70°N, 1.73°W) during the 11 August 1999 eclipse, which occurred under a low geomagnetic activity level. For this same eclipse, Le et al. (2008) used observations from a network containing 16 ionosondes (37.1–66.5°N) and simulation results from TIME-IGGCAS (a Chinese model). They found the following: (a) the $F1$ layer electron concentration decreases were more significant than the $F2$ layer decreases, even up to 2000 km; (b) the conjugate hemisphere exhibited slight decreases; and (c) the E region and F region synchronous electron concentrations decreased with time lags of 15, 60, and 30 min at altitudes of 300, 600, and 1,200 km, respectively, and the temperature decreased by up to 700 K at all altitudes ending 30 min after totality.

Afraimovich et al. (2002) also reported a summary of the ionospheric effects from eight solar eclipses (1970–1997) giving time delays relative to totality of 0–80 min and electron concentration decreases of 9×10^4 to $4 \times 10^6 \text{ cm}^{-3}$ and 0.1–14 TECu using measurements from ISR, vertical and oblique incidence sounders, and Faraday rotation of the VHF signals from geostationary satellite beacons. Moreover, summaries of ionosonde observations (40 stations) during 15 eclipses (1973–2006) and GPS TEC measurements (eight receivers) during six eclipses (1999–2006) in the Northern Hemisphere (0°–60°N) allowed Le, Liu, Yue, Wan, and Ning (2009) to determine the latitude dependence of the ionospheric responses ($NmF2$, TEC, and $hmF2$) to eclipses. These dependencies were compared with the results from the TIME-IGGCAS model. Although, in both cases, the latitudinal minima of $NmF2$ and TEC were found at middle latitudes (approximately 40°), there were significant differences between the model and observational dependencies.

Using simultaneous observations from four ionosondes (located in Spain, the Czech Republic, Belgium, and Germany), a differential Doppler system (composed of two transmitters and one receiver located in Spain) and GPS TEC measurements (from more than 100 receivers of the International GNSS Service over Europe and polar regions), Jakowski et al. (2008) reported the ionospheric effects of the 3 October 2005 solar eclipse over Spain. They found that the ionosphere responded by (a) an approximately 30% TEC decrease (as measured by GNSS TEC) resulting from an $NmF2$ decrease, an $hmF2$ increase, and an initial slab thickness increase and (b) a small-amplitude AGW with an approximately 60 min period. The former is probably associated with a competing slab thickness increase and regional cooling, while the latter has no clear source, that is, either in the thermosphere (~180 km altitude) or somewhere in the middle atmosphere.

The total solar eclipse on 1 August 2008 over the polar region was studied by Momani et al. (2010) using GPS TEC observations (14 receivers), magnetometers (3), and the three ISRs of the European EISCAT consortium.

They found 11–40% TEC decreases for all stations from the onset of solar corona obscuration until the end. Additionally, the electron concentration, electron temperature, ion velocity, and plasma frequency decreased, although the *E* and *F* layers responded differently. At two of the locations, the total geomagnetic field and the *X* and *Z* components showed decreases from 28 to 15 nT, while the *Y* component slightly increased from 18 to 22 nT. This eclipse was also examined by Domnin et al. (2013) and Burmaka and Chernogorb (2013) using the Kharkov ISR instrument. Over Kharkov (49.7°N; 36.3°E), *NmF2* and *foF2* decreased (32% and 17.5%, respectively), but *hmF2* did not significantly change, and both electron and ion temperatures decreased from 180–70 and 140–0 K at 190 and 490 km, respectively. Quasiperiodic disturbances of the electron concentration were also reported. The amplitudes ranged from 2×10^9 to 4×10^{10} , and the periods ranged within 20–25, 50–65, and 150–180 min for all altitudes in the 125–510 km range.

The ionospheric effects of the 22 July 2009 solar eclipse over China and India were reported by Chen, Zhao, Zhang, et al. (2011) and Kumar et al. (2013). Chen, Zhao, Zhang, et al. (2011) focused on the study of sporadic *Es* layer effects over Wuhan, China (30.4°N, 114.3°E), using simultaneous observations from an ionosonde (producing ionograms every 5 min) and an oblique backscattering sounding system (1 min resolution of the echo range and Doppler velocity measurements). They found the exceptional occurrence of the *Es* layer during the eclipse with a quasi-periodic periodicity of approximately 35 min for both the electron concentration and the spread *Es* drifting velocity. They suggested that an AGW deformed the *Es* layer and produced wave-like structures responsible for off-vertical *Es* echoes. The complementary observations of Kumar et al. (2013) over the Indian continent dealt with *vTEC* and *N(h)* derived from four low-latitude GPS locations (100% to 78% obscuration) and FORMOSAT-3/COSMIC satellite mission data, respectively. Their principal findings are as follows: (a) *vTEC* declined during the eclipse compared with the values observed during seven reference days (some before and after the eclipse); (b) TEC oscillations were observed with 40–120 min periods and were associated with an AGW generated in the lower atmosphere; and (c) *N(h)* was reduced at all heights (10%–48%) with a maximum reduction at 360 km.

Amabayo et al. (2014) investigated the response of the equatorial ionosphere to the solar eclipse on 3 November 2013. Four GPS receivers over East Africa (from 2.69° to 6.73°S geomagnetic latitude) were used. Both TEC enhancements and depletions were observed during the time of totality over all equatorial stations. The largest TEC perturbation amplitude of ≥ 20 TECu (18–20 UT) was observed at the southernmost station. Their study also included a wavelet analysis to determine the presence of wave-like structures and traveling ionospheric disturbances (TIDs). They assumed that the TEC perturbations (periods from 1.0–2.5 hr) were entirely due to the obscuration of solar UV radiation, which led to varying ionization levels in the ionosphere.

Pezzopane et al. (2015) showed how the partial solar eclipse (45–54% maximum obscuration) that occurred on 20 March 2015 influenced the sporadic *E* layer, as recorded by advanced ionospheric sounders in Rome (41.8°N, 12.5°E) and Gibilmanna (37.9°N, 14.0°E), Italy. The *ftEs* did not depend on strong thermal gradients, which were comparable between the previous day and the next day. In contrast, *Es* was rather persistent. The *Es* layer was always present near the solar eclipse time, both at Rome and Gibilmanna, contrary to what typically happens in March. A detailed analysis of isoheight ionogram plots suggests that TIDs likely caused by a GW played a significant role in causing the persistence of the *Es* layer.

For the total solar eclipse on 21 August 2017, the path of totality (approximately 100 km wide) traversed the central part of the continental United States from coast to coast in approximately 2 hr. There was broad coverage of ionospheric observations with an extremely high spatial resolution; these observations were available for the first time for an eclipse study. In fact, model predictions of the suggested effects on the time variations of the electron concentration, electron temperature, and oxygen ion velocity at different heights and on the TEC at a given place were available before the eclipse (Huba & Drob, 2017). Below, in turn, a single ionospheric station report, results from networks of stations, measurements using the Millstone Hill ISR, the use of extensive GNSS receiver observations, and posteclipse modeling and observational studies are presented.

Single station (34.8°N, 112.7°W) ionospheric observations in the vicinity of the totality path and corresponding modeling results have been published by Reinisch et al. (2018). They used digisonde records to determine the diurnal variations of *foE*, *foF1*, and *foF2* and to derive *hmE*, *hmF1*, and *hmF2* using the NHPC profile inversion program. The International Reference Ionosphere (IRI) model was used to calculate the same ionospheric variables. The simulated and observed *foE* and *foF1* almost coincided before and after the

eclipse. During the eclipse, foE and $foF1$ decreased and increased as expected according to the magnitude of obscuration. By contrast, the observed $foF2$ was smaller than the IRI values, both before and after the eclipse (for as much as 1 MHz). There was an $foF2$ effect during the obscuration period. However, this was not related to the magnitude of obscuration. Neither its shape nor its minimum value was attained.

Furthermore, a precise adjustment of $hmF2$ to obtain an appropriate $NmF2$ suggests that photochemical processes are more important than transport processes (winds). Moreover, the field line interhemispheric plasma (FLIP) model was used to analyze $N(h)$ and the time variations of $hmF2$. Comparisons with the FLIP results show modeled $NmF1$ values larger than $NmF2$ between 30 and 60 min after the eclipse. Alternatively, Adekoya et al. (2019) determined the effect of the solar eclipse using a network of digisondes covering locations north of the totality band (Millstone Hill), near the northern fringe of the totality band (Boulder), within the totality band (Idaho), near the southern fringe of the totality band (Eglin), 90% obscuration (Point Arguello), and south of the totality band (Austin). They found a decrease in electron density during the eclipse attributed to the reduced solar radiation and neutral gas heating. The maximum obscuration consistently coincided with an increase in $hmF2$ and with a lagged maximum decrease in $NmF2$ at the stations investigated.

Detailed observations of the eclipse impacts at different altitudes were reported by Goncharenko et al. (2018) using the incoherent scatter technique together with a collocated digisonde at Millstone Hill (42.6° N, 71.5° E) with a maximum obscuration of 63%. Radar measurements were obtained during a total of 5 days prior, during, and after the eclipse. The electron density results were compared with an empirical model and observations on 22 August 2017, which was selected as the eclipse control (reference) day. The results indicated a 30–40% maximum decrease in electron density in the $F2$ layer (200–300 km altitude) during the maximum obscuration. Alternatively, the electron and ion temperatures compared with those predicted by the empirical model showed decreases above 150 km of 100 to 220 and 50 to 140 K, respectively. A remarkable observation of upward plasma drift with an increase of 20 to 40 m s^{-1} was obtained above the $F2$ peak (~250 km) after the maximum obscuration. This increase was the first report of possible upward plasma transport generated by an eclipse.

One of the early reports on this eclipse with a large set of observations was presented by Zhang et al. (2017). They assembled observations from ~2,000 GNSS receivers to derive the TEC over North America and found what they called “unambiguous evidence” of ionospheric bow waves lasting approximately 1 hr with a wavelength of 300–400 km and a phase speed of ~280 m s^{-1} originating from the totality region. Furthermore, they noted supersonic ionospheric perturbations from the maximum solar obscuration, which were too fast to be associated with GWs or TIDs. Similar analyses by Sun et al. (2018) indicated that a “great ionospheric bow wave front” (~3,000 km wide) was observed. The supersonic moon shadow-induced acoustic shock wave resulted in the bow wave trough and crest near the totality path. The acoustic shock wave and plasma recombination in the ionosphere controlled the formation of the bow wave front rather than AGWs excited by the moon shadow from the lower atmosphere. These findings seem to be substantiated by modeling the eclipse’s atmospheric effects using the Global Ionosphere-Thermosphere Model (GITM, Lin et al., 2018). By contrast, Mrak, Semeter, Drob, et al. (2018) and Mrak, Semeter, Nishimura, et al. (2018) suggested that (a) the TEC observations and modeling results can be explained by the coincidental production of TIDs by tropospheric storm waves that propagate radially from the storm center with a horizontal wavelength of ~350 km and a velocity of ~200 m s^{-1} and that (b) the prominent large-scale TEC disturbances are produced by direct EUV modulation due to the inhomogeneity of solar radiation.

Furthermore, Eisenbeis et al. (2019), using 3,000 GNSS receivers to determine the TEC, found that a 3-D fast Fourier transform analysis permits the full identification of TIDs generated by an eclipse. They found that these TIDs exhibit wavelengths and periods of 50–100 km and 30 min, respectively, and 500–600 km and 65 min. Moreover, they suggested that these TIDs are what other researchers have identified as bow waves.

Similar TEC observations using more than 3,600 GNSS receivers were reported by He et al. (2018). By using an involved 3-D ionospheric density reconstruction procedure, they found the peak depletion at 200 km and 40%, 60%, and 72% depletions at 250, 350, and 450 km, respectively. The integral density depletion between 150 and 450 km amounted to 54%. These depletions were validated above 200 km using the results of ISR observations from Millstone Hill (Goncharenko et al., 2018) and at 400 km with in situ Swarm satellite mission determinations. The above mentioned authors also detected depletions and enhancements at the

geomagnetic conjugate locations of the eclipse in the Southern Hemisphere using this methodology, in concordance with the results of Huba and Drob (2017).

Some modeling and observational studies (Aryal et al., 2019; Lei et al., 2018) concentrated on the posteclipse ionospheric response. Lei et al. (2018) found small global average TEC perturbations (0.2 TECu) 9 hr after an eclipse. Alternatively, multiinstrument (GNSS TEC and digisonde) and spectral observations (OI emissions) led Aryal et al. (2019) to conclude that it is the prevalent geomagnetic disturbance via enhanced auroral currents/Joule heating that generates AGWs and large-scale traveling ionospheric disturbances (LSTIDs) propagating toward the equator. GITM results show that the associated 10% increases in N and O/N₂ at 250 km present oscillations of 90 min with vertical speeds and wavelengths of 7 m s⁻¹ and 36 km, respectively, and 616 m s⁻¹ and 1,256 km.

Appendix B: The IPS-42 Ionosonde and the New Registration and Scaling Systems

The IPS-42 ionosonde was designed in 1974 by the Australian Ionospheric Prediction Service and commercially produced in 1979 by KEL Aerospace Pty Ltd. of Australia under the leadership of Terry Kelly (Wilkinson et al., 2018). This ionosonde transmits at 576 frequencies logarithmically spaced between 1 and 22.6 MHz in sweeps of 12 s. The transmissions at each frequency consist of three pulses of 41.7 μs, which are separated from each other by 5.33 ms, each with a bandwidth equal to 25 kHz. In the original design, the signals recorded by the ionosonde are visualized as dots formed in a cathode-ray tube screen. The recording of each point on the screen was achieved by a 16 mm camera whose shutter remained open for 12 s. In later versions of the equipment, the data were acquired digitally using DOS code (the Auckland University DIGION system) designed by Titheridge (1994a). Due to the failure of the digital acquisition system several weeks before the eclipse and because the original camera was no longer available, a new registration system was developed.

An 8 megapixel Raspberry Pi digital camera was attached to the IPS-42 monitor screen and operated using a Raspberry Pi computer. A small 3-D-printed structure was designed to support the computer and the camera centered over the screen with a final distance between the camera lens and screen of approximately 7 cm. The general-purpose input-output (GPIO) pins of the Raspberry Pi (Upton & Halfacree, 2016) were used to trigger a switch for the old camera system activation signal, which dropped from 5 to 0 V just 2 s before an ionogram sequence was initiated. This signal switch was used to launch a video capture of each scan. The captured video was subsequently converted to an image of an ionogram. This image conversion was performed by adding the frames of each video to a grayscale image and using different perspective corrections and morphological operations to reduce the error of each ionogram to a minimum, obtaining a virtual height estimation uncertainty identical to the default IPS-42 height error (± 5 km).

Obtained ionograms were reduced using a new scaling tool, Digitized Ionogram Scaling Software (DISS; Urra, 2019). DISS is a MATLAB script based on the same principles of DIGION software (Titheridge, 1994a), allowing data to be acquired by manually scaling 12 variables from the E and F layers, with qualifying/descriptive letters following the proper accuracy rules. This software uses the pixel-to-frequency relationship described in the DIGION manual (Titheridge, 1994b) to avoid selecting frequencies and virtual heights that are not practically feasible by the ionosonde electronics.

Data Availability Statement

The ionosonde data used and the numerical model outputs are available online (<https://www2.dgeo.udec.cl/IONO/Eclipse>).

References

- Adekoya, B. J., Adebesein, B. O., David, T. W., Ikubanni, S. O., Adebiji, S. J., Bolaji, O. S., & Chukwuma, V. U. (2019). Solar-eclipse-induced perturbations at mid-latitude during the 21 August 2017 event. *Annales de Geophysique*, 37(2), 171–182. <https://doi.org/10.5194/angeo-37-171-2019>
- Adekoya, B. J., Chukwuma, V. U., & Reinisch, B. W. (2015). Ionospheric vertical plasma drift and electron density response during total solar eclipses at equatorial/low latitude. *Journal of Geophysical Research: Space Physics*, 120, 8066–8084. <https://doi.org/10.1002/2015JA021557>

Acknowledgments

Access to the ionograms from Tucumán was provided by the Low-Latitude Ionospheric Sensor Network (LISN, <http://lisn.igp.gob.pe/>). Access to the ionograms from Jicamarca was provided by DIDbase (<https://ulcar.uml.edu/DIDBase/>). Access to the GPS data was kindly provided by the International GNSS Service (IGS, www.igs.org, Dow et al., 2009), by the Centro Sismológico Nacional (CSN) of the Universidad de Chile (www.sismologia.cl), by the Red Argentina de Monitoreo Satelital Continuo (RAMSAC) of the Instituto Geográfico Nacional de la República Argentina (www.ign.gob.ar, Piñón et al., 2018), by the Rede Brasileira de Monitoramento Continuo dos Sistemas GNSS (RBMC) of the Instituto Brasileiro de Geografia e Estatística (www.ibge.gov.br), by the Red Geodésica Nacional Activa (REGNA) of the Instituto Geográfico Militar del Uruguay (<ftp://pp.igm.gub.uy>), and by Marco Geocentrico Nacional de Referencia (MAGNA) of the Instituto Geográfico Agustín Codazzi, Colombia (<https://geoportal.igac.gov.co/>). M. Bravo acknowledges the support by CONICYT/FONDECYT POSTDOCTORADO 3180742. M. Martínez-Ledesma acknowledges the AFOSR Project FA9550-19-1-0384. J. R. Souza would like to thank the CNPq (under Grant 307181/2018-9) for research productivity sponsorship and the INCT GNSS-NavAer supported by CNPq (465648/2014-2), FAPESP (2017/50115-0), and CAPES (88887.137186/2017-00). P. R. Muñoz acknowledges DIDULS for financial support. One GNSS receiver was provided by Marina Stepanova through project AFOSR FA9550-1-0139. The authors wish to thank the reviewers, in particular P. Richards, for their assistance in evaluating this paper.

- Afraimovich, E. L., Kosogorov, E. A., & Lesyuta, O. S. (2002). Effects of the August 11, 1999 total solar eclipse as deduced from total electron content measurements at the GPS network. *Journal of Atmospheric and Solar-Terrestrial Physics*, *64*(18), 1933–1941. [https://doi.org/10.1016/s1364-6826\(02\)00221-3](https://doi.org/10.1016/s1364-6826(02)00221-3)
- Amabayo, E. B., Anguma, S. K., & Jurua, E. (2014). Tracking the ionospheric response to the solar eclipse of November 03, 2013. *International Journal of Atmospheric Sciences*, *2014*, 1–10. <https://doi.org/10.1155/2014/127859>
- Anderson, D., Anghel, A., Chau, J., & Veliz, O. (2004). Daytime vertical $E \times B$ drift velocities inferred from ground-based magnetometer observations at low latitudes. *Space Weather*, *2*, S11001. <https://doi.org/10.1029/2004SW000095>
- Aryal, S., Geddes, G., Fin, S. C., Mrak, S., Galkin, I., Cnossen, I., et al. (2019). Multi-spectral and multi instrument observation of TIDs following the Total Solar Eclipse of August 21. *Journal of Geophysical Research: Space Physics*, *124*, 3761–3774. <https://doi.org/10.1029/2018JA026333>
- Bailey, G. J., & Sellek, R. (1990). A mathematical model of the Earth's plasmasphere and its application in a study of He at $L = 3$. *Annales de Geophysique*, *8*(3), 171–189.
- Bailey, G. J., Sellek, R., & Rippeth, Y. (1993). A modelling study of the equatorial topside ionosphere. *Annales de Geophysique*, *11*(4), 263–272.
- Bates, D. R., & McDowell, M. R. C. (1957). Recombination in the ionosphere during an eclipse. *Journal of Atmospheric and Terrestrial Physics*, *10*(2), 96–102. [https://doi.org/10.1016/0021-9169\(57\)90143-5](https://doi.org/10.1016/0021-9169(57)90143-5)
- Beynon, W. J. G. (1955). Solar eclipses and the ionosphere. *Nature*, *176*(4490), 947–948. <https://doi.org/10.1038/176947a0>
- Bowhill, S. A. (1961). The effective recombination coefficient of an ionosphere containing a mixture of ions. *Journal of Atmospheric and Terrestrial Physics*, *20*(1), 19–30. [https://doi.org/10.1016/0021-9169\(61\)90094-0](https://doi.org/10.1016/0021-9169(61)90094-0)
- Bravo, M. A., Batista, I. S., Souza, J. R., & Foppiano, A. J. (2017). Equatorial Ionospheric Response to Different Estimated Disturbed Electric Fields as Investigated Using Sheffield University Plasmasphere Ionosphere Model at INPE. *Journal of Geophysical Research: Space Physics*, *122*, 10,511–10,527. <https://doi.org/10.1002/2017JA024265>
- Bravo, M. A., Batista, I. S., Souza, J. R., & Foppiano, A. J. (2019). Ionospheric response to disturbed winds during the 29 October 2003 geomagnetic storm in the Brazilian sector. *Journal of Geophysical Research: Space Physics*, *124*, 9405–9419. <https://doi.org/10.1029/2019JA027187>
- Burmaka, V. P., & Chernogorb, L. F. (2013). Solar eclipse of August 1, 2008, above Kharkov: 2. Observation results of wave disturbances in the ionosphere. *Geomagnetism and Aeronomy*, *53*(4), 479–491. <https://doi.org/10.1134/S001679321304004X>
- Chandra, H., Sharma, S., Lele, P. D., Rajaram, G., & Hanchinal, A. (2007). Ionospheric measurements during the total solar eclipse of 11 August 1999. *Earth, Planets and Space*, *59*(1), 59–64. <https://doi.org/10.1186/BF03352023>
- Chen, G., Zhao, Z., Ning, B., Deng, Z., Yang, G., Zhou, C., et al. (2011). Latitudinal dependence of the ionospheric response to solar eclipse of 15 January 2010. *Journal of Geophysical Research*, *116*, A06301. <https://doi.org/10.1029/2010JA016305>
- Chen, G., Zhao, Z., Zhang, Y., Yang, G., Zhou, C., Huang, S., et al. (2011). Gravity waves and spread E_s observed during the solar eclipse of 22 July 2009. *Journal of Geophysical Research*, *116*, A09314. <https://doi.org/10.1029/2011JA016720>
- Cheng, K. H., Huang, Y. N., & Chen, S. W. (1992). Ionospheric effects of the solar eclipse of September 23, 1987, around the equatorial anomaly crest region. *Journal of Geophysical Research*, *97*(A1), 103–111. <https://doi.org/10.1029/91JA02409>
- Cherniak, I. V., & Lysenko, V. N. (2013). Measurements of the ionosphere plasma electron density variation by the Kharkov Incoherent Scatter Radar. *Acta Geophysica*, *61*(5), 1289–1303. <https://doi.org/10.2478/s11600-013-0118-0>
- Chukwuma, V. U., & Adekoya, B. J. (2016). The effects of March 20 2015 solar eclipse on the F2 layer in the mid-latitude. *Advances in Space Research*, *58*(9), 1720–1731. <https://doi.org/10.1016/j.asr.2016.06.038>
- De Jager, G., & Gledhill, J. A. (1963). The enhancement of the F1-cusp and the appearance of the F1.5-layer during solar eclipses. *Journal of Atmospheric and Terrestrial Physics*, *25*, 403–414.
- Domnin, I. F., Yemel'yanov, L. Y., Kotov, D. V., Lyashenko, M. V., & Chernogor, L. F. (2013). Solar Eclipse of August 1, 2008, above Kharkov: 1. Results of Incoherent Scatter Observations. *Geomagnetism and Aeronomy*, *53*, 113–123. <https://doi.org/10.1134/S0016793213010076>
- Dow, J. M., Neilan, R. E., & Rizos, C. (2009). The International GNSS Service in a changing landscape of Global Navigation Satellite Systems. *Journal of Geodesy*, *83*(3–4), 191–198. <https://doi.org/10.1007/s00190-008-0300-3>
- Eccles, J. V., St. Maurice, J. P., & Schunk, R. W. (2015). Mechanisms underlying the prereversal enhancement of the vertical plasma drift in the low-latitude ionosphere. *Journal of Geophysical Research: Space Physics*, *120*, 4950–4970. <https://doi.org/10.1002/2014JA020664>
- Eisenbeis, J., Occhipinti, G., Astafyeva, E., & Rolland, L. (2019). Short- and long-wavelength TIDs generated by the Great American Eclipse of 21 August 2017. *Journal of Geophysical Research: Space Physics*, *124*, 9486–9493. <https://doi.org/10.1029/2019JA026919>
- Evans, J. V. (1965a). An F-region eclipse. *Journal of Geophysical Research*, *70*(1), 131–142. <https://doi.org/10.1029/JZ070i001p00131>
- Evans, J. V. (1965b). On the behavior of foF_2 during solar eclipses. *Journal of Geophysical Research*, *70*(3), 733–738. <https://doi.org/10.1029/JZ070i003p00733>
- Fejer, B. G., Jensen, J. W., & Su, S.-Y. (2008). Quiet time equatorial F region vertical plasma drift model derived from ROCSAT-1 observations. *Journal of Geophysical Research*, *113*, A05304. <https://doi.org/10.1029/2007JA012801>
- Frissell, N. (2017). w2naf/eclipse_calculator v1.0 (Version v1.0). Zenodo. <https://doi.org/10.5281/zenodo.1120440>
- Goncharenko, L. P., Erickson, P. J., Zhang, S. R., Galkin, I., Coster, A. J., & Jonah, O. F. (2018). Ionospheric response to the solar eclipse of 21 August 2017 in Millstone Hill (42N) observations. *Geophysical Research Letters*, *45*, 4601–4609. <https://doi.org/10.1029/2018GL077334>
- He, L., Heki, K., & Wu, L. (2018). Three-dimensional and trans-hemispheric changes in ionospheric electron density caused by the great solar eclipse in North America on 21 August 2017. *Geophysical Research Letters*, *45*, 10,933–10,940. <https://doi.org/10.1029/2018GL080365>
- Hedin, A. E., Fleming, E. L., Manson, A. H., Schmidlin, F. J., Avery, S. K., Clark, R. R., et al. (1996). Empirical wind model for the upper, middle and lower atmosphere. *Journal of Atmospheric and Terrestrial Physics*, *58*(13), 1421–1447. [https://doi.org/10.1016/0021-9169\(95\)00122-0](https://doi.org/10.1016/0021-9169(95)00122-0)
- Higgs, A. J. (1942). Ionospheric measurements made during the total solar eclipse of 1940 October 1. *Monthly Notices of the Royal Astronomical Society*, *102*(1), 24–34. <https://doi.org/10.1093/mnras/102.1.24>
- Huba, J. D., & Drob, D. (2017). SAMI3 prediction of the impact of the 21 August 2017 total solar eclipse on the ionosphere/plasmasphere system. *Geophysical Research Letters*, *44*, 5928–5935. <https://doi.org/10.1002/2017GL073549>
- Huba, J. D., Joyce, G., & Fedder, J. A. (2000). Sami2 is Another Model of the Ionosphere (SAMI2): A new low-latitude ionosphere model. *Journal of Geophysical Research*, *105*(A10), 23,035–23,053. <https://doi.org/10.1029/2000JA000035>
- Jakowski, N., Stankov, S. M., Wilken, V., Borries, C., Altadill, D., Chum, J., et al. (2008). Ionospheric behavior over Europe during the solar eclipse of 3 October 2005. *Journal of Atmospheric and Solar-Terrestrial Physics*, *70*(6), 836–853. <https://doi.org/10.1016/j.jastp.2007.02.016>

- Kelley, M. C. (2009). *The Earth's ionosphere: Plasma physics & electrodynamics*. San Diego, CA: Academic Press.
- Kumar, S., Singh, A. K., & Singh, R. P. (2013). Ionospheric response to total solar eclipse of 22 July 2009 in different Indian regions. *Annales de Geophysique*, 31(9), 1549–1558. <https://doi.org/10.5194/angeo-31-1549-2013>
- Le, H., Liu, L., Yue, X., & Wan, W. (2008). The ionospheric responses to the 11 August 1999 solar eclipse: Observations and modeling. *Annals of Geophysics: Atmospheres, Hydrospheres and Space Sciences*, 26(1), 107. <https://doi.org/10.5194/angeo-26-107-2008>
- Le, H., Liu, L., Yue, X., & Wan, W. (2009). The ionospheric behavior in conjugate hemispheres during the 3 October 2005 solar eclipse. *Annales de Geophysique*, 27(1), 179–184. <https://doi.org/10.5194/angeo-27-179-2009>
- Le, H., Liu, L., Yue, X., Wan, W., & Ning, B. (2009). Latitudinal dependence of the ionospheric response to solar eclipses. *Journal of Geophysical Research*, 114, A07308. <https://doi.org/10.1029/2009JA014072>
- Lei, J., Dang, T., Wang, W., Burns, A., Zhang, B., & Le, H. (2018). Long-lasting response of the global thermosphere and ionosphere to the 21 August 2017 solar eclipse. *Journal of Geophysical Research: Space Physics*, 123, 4309–4316. <https://doi.org/10.1029/2018JA025460>
- Lerfeld, G. M., Hargreaves, J. K., & Watts, J. M. (1965). D-region absorption at 10 and 15 mc/s during the total solar eclipse of July 20, 1963. *Radio Science*, 69D(7), 939–946.
- Lin, C. Y., Deng, Y., & Ridley, A. (2018). Atmospheric gravity waves in the ionosphere and thermosphere during the 2017 solar eclipse. *Geophysical Research Letters*, 45, 5246–5252. <https://doi.org/10.1029/2018GL077388>
- Mansoori, A. A., Parvaiz, A., Khan, P. A., Bhawre, P., Purohit, P. K., & Gwal, A. K. (2011). Solar eclipses and ionospheric effects: Some historical perspectives. *International Journal of Geomatics and Geosciences*, 1(4), 662–668. ISSN 0976–4380
- Mitra, S. K., Rakshit, H., Syam, P., & Ghose, B. N. (1933). Effect of the solar eclipse on the ionosphere. *Nature*, 132(3333), 442–443. <https://doi.org/10.1038/132442a0>
- Momani, M. A., Yatim, B., & Mohd Ali, M. A. (2010). Ionospheric and geomagnetic response to the total solar eclipse on 1 August 2008 over Northern Hemisphere. *Journal of Geophysical Research*, 115, A08321. <https://doi.org/10.1029/2009JA014999>
- Mrak, S., Semeter, J., Nishimura, Y., Hirsch, M., & Sivasdas, N. (2018). Coincidental TID production by tropospheric weather during the August 2017 total solar eclipse. *Geophysical Research Letters*, 45, 10,903–10,911. <https://doi.org/10.1029/2018GL080239>
- Mrak, S., Semeter, J. L., Drob, D., & Huba, J. D. (2018). Direct EUV/X-ray modulation of the ionosphere during the August 2017 total solar eclipse. *Geophysical Research Letters*, 45, 3820–3828. <https://doi.org/10.1029/2017GL076771>
- Nogueira, P. A. B., Abdu, M. A., Souza, J. R., Bailey, G. J., Batista, I. S., Shume, E. B., & Denardini, C. M. (2013). Longitudinal variation in Global Navigation Satellite Systems TEC and topside ion density over South American sector associated with the four-peaked wave structures. *Journal of Geophysical Research: Space Physics*, 118, 7940–7953. <https://doi.org/10.1002/2013JA019266>
- Pezzopane, M., Pietrella, M., Pignalberi, A., & Tozzia, R. (2015). 20 March 2015 solar eclipse influence on sporadic E layer. *Advances in Space Research*, 56(10), 2064–2072. <https://doi.org/10.1016/j.asr.2015.08.001>
- Picone, J. M., Hedin, A. E., Drob, D. P., & Aikin, A. C. (2002). NRLMSISE-00 empirical model of the atmosphere: Statistical comparisons and scientific issues. *Journal of Geophysical Research*, 107(A12), 1468. <https://doi.org/10.1029/2002JA009430>
- Piggott, W. R., & Rawer, K. (Eds.) (1972). *WDC. URSI. Handbook of ionogram interpretation and reduction* (2nd ed.). Boulder, Colorado, USA: NOAA. World data Center a for solar-terrestrial physics report UAG-23A, November.
- Piñón, D. A., Gómez, D. D., Smalley, R., Cimbaro, S. R., Lauría, E. A., & Bevis, M. G. (2018). The history, state, and future of the Argentine continuous satellite monitoring network and its contributions to geodesy in Latin America. *Seismological Research Letters*, 89(2A), 475–482. <https://doi.org/10.1785/0220170162>
- Ratcliffe, J. A. (1956). A survey of solar eclipses and the ionosphere. In W. J. G. Beynon & G. M. Brown (Eds.), *Solar eclipses and the ionosphere* (pp. 1–13). Oxford: Pergamon Press.
- Reinisch, B. W., Dandenaull, P. B., Galkin, I. A., Hamel, R., & Richards, P. G. (2018). Investigation of the electron density variation during the 21 August 2017 solar eclipse. *Geophysical Research Letters*, 45, 1253–1261. <https://doi.org/10.1002/2017GL076572>
- Richards, P. G., Fennelly, J. A., & Torr, D. G. (1994). EUVAC: A solar EUV flux model for aeronomic calculations. *Journal of Geophysical Research*, 99(A5), 8981–8992. <https://doi.org/10.1029/94JA00518>
- Rishbeth, H. (1968). Solar eclipses and ionospheric theory. *Space Science Reviews*, 8(4), 543–554. <https://doi.org/10.1007/BF00175006>
- Rishbeth, H., & Garriot, O. K. (1969). *Introduction to ionospheric physics*, 193–199. New York & London: Academic Press.
- Salah, J. E., Oliver, W. L., Foster, J. J., Holt, J. M., Emery, B. A., & Roble, R. G. (1986). Observation of the May 30, 1984, annular solar eclipse at Millstone Hill. *Journal of Geophysical Research*, 91(A2), 1651–1660. <https://doi.org/10.1029/JA091iA02p01651>
- Santos, A. M., Abdu, M. A., Souza, J. R., Sobral, J. H. A., & Batista, I. S. (2016). Disturbance zonal and vertical plasma drifts in the Peruvian sector during solar minimum phases. *Journal of Geophysical Research: Space Physics*, 121, 2503–2521. <https://doi.org/10.1002/2015JA022146>
- Seemala, G. K., & Valladares, C. E. (2011). Statistics of total electron content depletions observed over the south American continent for the year 2008. *Radio Science*, 46, RS5019. <https://doi.org/10.1029/2011RS004722>
- Sergeenko, N. P. (2018). Irregular phenomena in magnetically conjugate regions of the F2 layer of the ionosphere. *Geomagnetism and Aeronomy*, 58(6), 823–830. <https://doi.org/10.1134/S0016793218060166>
- Souza, J., Brum, C., Abdu, M., Batista, I., Asevedo, W., Bailey, G., & Bittencourt, J. (2010). Parameterized regional ionospheric model and a comparison of its results with experimental data and IRI representations. *Advances in Space Research*, 46(8), 1032–1038. <https://doi.org/10.1016/j.asr.2009.11.025>
- Souza, J. R., Asevedo, W. D. Jr., dos Santos, P. C. P., Petry, A., Bailey, G. J., Batista, I. S., & Abdu, M. A. (2013). Longitudinal variation of the equatorial ionosphere: Modeling and experimental results. *Advances in Space Research*, 51(4), 654–660. <https://doi.org/10.1016/j.asr.2012.01.023>
- Sridharan, R., Devasia, C. V., Jyoti, N., Tiwari, D., Viswanathan, K. S., & Subbarao, K. S. V. (2002). Effects of solar eclipse on the electro-dynamical processes of the equatorial ionosphere: A case study during 11 August 1999 dusk time total solar eclipse over India. *Annales de Geophysique*, 20(12), 1977–1985. <https://doi.org/10.5194/angeo-20-1977-2002>
- Stankov, S. M., Bergeot, N., Berghmans, D., Bolsée, D., Bruyninx, C., Chevalier, J.-M., et al. (2017). Multi-instrument observations of the solar eclipse on 20 March 2015 and its effects on the ionosphere over Belgium and Europe. *Journal of Space Weather Space Climate*, 7, A19. <https://doi.org/10.1051/swsc/2017017>
- Strobel, D. F., Young, T. R., Meier, R. R., Coffey, T. P., & Ali, A. W. (1974). The nighttime ionosphere: E region and lower F region. *Journal of Geophysical Research*, 79(22), 3171–3178. <https://doi.org/10.1029/JA079i022p03171>
- Sun, Y.-Y., Liu, J.-Y., Lin, C.-H., Lin, C.-Y., Shen, M.-H., Chen, C.-H., et al. (2018). Ionospheric bow wave induced by the moon shadow ship over the continent of United States on 21 August 2017. *Geophysical Research Letters*, 45, 538–544. <https://doi.org/10.1002/2017GL075926>
- Szendrei, M. E., & McElhinny, M. W. (1956). Recombination and attachment in the F1 and F2 layers during the solar eclipse of 25 December 1954. *Journal of Atmospheric and Terrestrial Physics*, 9(2–3), 118–130. [https://doi.org/10.1016/0021-9169\(56\)90171-4](https://doi.org/10.1016/0021-9169(56)90171-4)

- Titheridge, J. E. (1994a). Computer control of an IPS-42 Ionosonde. INAG (Ionosonde Network Advisory Group) bulletin, 60. Available at: <http://www.sws.bom.gov.au/IPSHosted/INAG/web-60/digion.htm> (last access: 14 Oct. 2019)
- Titheridge, J. E. (1994b). Manual for the A.U. DIGION system. Version 3.1, of March 1994. Available at: https://www.sws.bom.gov.au/IPSHosted/INAG/files/4b24d_digion_manual.pdf (last access: 18 Oct. 2019)
- Tobiska, W., Woods, T., Eparvier, F., Viereck, R., Floyd, L., Bouwer, D., et al. (2000). The SOLAR2000 empirical SOLAR irradiance model and forecast tool. *Journal of Atmospheric and Solar-Terrestrial Physics*, 62(14), 1233–1250. [https://doi.org/10.1016/S1364-6826\(00\)00070-5](https://doi.org/10.1016/S1364-6826(00)00070-5)
- Upton, E., & Halfacree, G. (2016). *Raspberry Pi user guide*. Chichester, West Sussex, UK: John Wiley & Sons. ISBN: 978-1-119-26436-1
- Urra, B. (2019). Digitized Ionogram Scaling Software, <https://github.com/CInFAA/DISS>
- Verhulst, T. G. W., & Stankov, S. M. (2020). Height dependency of solar eclipse effects: The ionospheric perspective. *Journal of Geophysical Research: Space Physics*, 125, e2020JA028088. <https://doi.org/10.1029/2020JA028088>
- Wilkinson, P., Kennewell, J. A., & Cole, D. (2018). The development of the Australian Space Forecast Centre (ASFC). *History of Geophysical and Space Science*, 9(1), 53–63. <https://doi.org/10.5194/hgss-9-53-2018>
- Wireless World (1932). The wireless eclipse. *Wireless World*, 31, 141–142; August 19.
- Zhang, S.-R., Erickson, P. J., Goncharenko, L. P., Coster, A. J., Rideout, W., & Vierinen, J. (2017). Ionospheric bow waves and perturbations induced by the 21 August 2017 solar eclipse. *Geophysical Research Letters*, 44, 12,067–12,073. <https://doi.org/10.1002/2017GL076054>
- Zirker, J. B. (1980). Total eclipses of the Sun. *Science*, 210(4476), 1313–1319. <https://doi.org/10.1126/science.210.4476.1313>